Hindawi
Mathematical Problems in Engineering
Volume 2017, Article ID 6492081, 33 pages
https://doi.org/10.1155/2017/6492081

Research Article

A Refined Higher-Order Hybrid Stress Quadrilateral Element for Free Vibration and Buckling Analyses of Reissner-Mindlin Plates

Tan Li,[1] Xu Ma,[1] Wanji Chen,[2] and Xili Jing[1]

[1]*School of Science, Yanshan University, Qinhuangdao 066004, China*
[2]*Key Laboratory of Liaoning Province for Composite Structural Analysis of Aerocraft and Simulation, Shenyang Aerospace University, Shenyang 110136, China*

Correspondence should be addressed to Xu Ma; maxu824@ysu.edu.cn

Received 3 July 2017; Revised 20 September 2017; Accepted 6 November 2017; Published 27 November 2017

Academic Editor: Giovanni Garcea

This paper is devoted to develop a new 8-node higher-order hybrid stress element (QH8) for free vibration and buckling analysis based on the Mindlin/Reissner plate theory. In particular, a simple explicit expression of a refine method with an adjustable constant is introduced to improve the accuracy of the analysis. A combined mass matrix for natural frequency analysis and a combined geometric stiffness matrix for buckling analysis are obtained using the refined method. It is noted that numerical examples are presented to show the validity and efficiency of the present element for free vibration and buckling analysis of plates. Furthermore, satisfactory accuracy for thin and moderately thick plates is obtained and it is free from shear locking for thin plate analysis and can pass the nonzero shear stress patch test.

1. Introduction

It is well-known that the finite element method for free vibration and buckling analysis of plates is highly significant in civil, mechanical, and aerospace engineering applications. The patch test [1], which can be used to examine the convergence of the element and construct a convergence element, has been seen as a criterion for assessing the convergence of the finite element for a long time.

The potential energy function of Mindlin plate element contains the displacements and the first-order derivatives of the displacements. According to the C^0 continuity condition, it is quite easy to establish interpolation functions of deflection and rotation. Historically, the displacement-based approach was the first attempt in the formulation of effective Mindlin plate bending elements [2]. However, as we all know, the original displacement element tends to cause the shear-locking phenomenon which induces overstiffness as the plate becomes progressively thinner for low-order interpolation polynomials in the Mindlin elements. During this time, the convergence characteristics of the Mindlin plate elements were performed by means of numerical computation of pure bending and pure torsion [3, 4]. In order to avoid shear locking, various numerical techniques and effective modifications have been proposed and tested, such as the reduced integration and selective reduced integration schemes proposed by Zienkiewicz et al. [5], Pugh et al. [6], and Hughes et al. [7]; assumed natural strain method introduced by Hughes and Tezduyar [8]. It is acknowledged that the methods of reduced integration and selective integration are efficient approaches to prevent the appearance of the shear-locking phenomenon. However, it is found that such elements often exhibit extra zero-energy modes and also produce oscillatory results for some problems. Moreover, these solutions are not applicable to very thin plate; the thickness/span ratio of the plate is about restricted to 10^{-6}.

Later, Belytschko et al. [9] proposed the stabilization procedure to remove the zero-energy modes by perturbing the stiffness. In addition, several efficient 9-DOF triangular elements based on the discrete Kirchhoff constraint and the equilibrium conditions were developed by Batoz et al. [10, 11]. These elements can eliminate locking phenomenon and converge towards the discrete Kirchhoff plate bending elements when the thickness of the plate is very thin. On the other

hand, no element is free of shear locking in theory. Bathe et al. [12] introduced the MITC element and proposed strain energy patch test function to evaluate the convergence. Based on Timoshenko beam function, Soh et al. [13] proposed a triangular 9-DOF plate bending element which can be employed to analyze very thin plate (the thickness/span ratio of the plate is about 10^{-11}). Soon, Soh et al. [14] introduced a quadrilateral 12-DOF plate bending element. At this time, the progressively thinner plate which has the thickness/span ratio 10^{-20} can be calculated. Wanji and Cheung [15] proposed the zero shear stress patch test functions. It is apparent that this patch test is more rigorous than the patch test using numerical computation of pure bending and pure torsion of a small-scale plate. Then, elements such as RDKQM [15], RDKTM [16], AC-MQ4 [17], and QC-P4 [18] that can pass the above patch test functions were proposed, indicating that the shear-locking problem is solved. All these elements can be used to solve the extremely thin plate problem (the thickness/span ratio of the plate can reach to 10^{-30}). In other words, these elements can accurately converge to thin plate finite element solution.

Chen proposed the enhanced patch test [19] and presented the zero shear deformation patch test and nonzero constant shear deformation test functions of Mindlin plate [20]. Current patch test for Mindlin plate only satisfies the zero shear deformation condition. The patch test of nonzero constant shear for Mindlin plate problem cannot be performed. The convergence test should be performed during the process of developing finite element method. Only passing the rigorous nonzero constant shear stress patch test, the convergence can be completely guaranteed. The programs of this commercial software have no proof of convergence. The enhanced patch test is stronger than the original test; the original constant stress patch test is just a special case of it. This paper is devoted to establish Mindlin plate element which can pass the strict constant shear patch test.

Different from the classical Timoshenko beam function, Jelenić and Papa [21] proposed a new arbitrary-order Timoshenko beam function in 2011. So far, it is the only function which can be used to construct the functions of nonzero constant shear patch test for thick beam element. Since beam function can be regarded as a function on the boundary, the adopted hybrid stress method just requires the boundary function rather compared to the domain function. Because this beam function is arbitrary order, thus it has high enough order to perform the nonzero constant shear stress patch test. Since a complete cubic polynomial for the element function to pass the constant shear stress patch test is required, it was used to develop the higher-order hybrid stress triangular Mindlin plate bending element named TH6 [22] and quadrilateral Mindlin plate bending element named QH8 [23]. The results of static analysis have proved that the TH6 element and QH8 element can pass the rigorous nonzero constant shear stress patch test and its accuracy is quite high. Only passing the rigorous nonzero constant shear stress patch test, the convergence can be completely guaranteed.

The purpose of this paper is to develop an 8-node Mindlin plate bending finite element for free vibration analysis and buckling analysis within an assumed stress formulation, whose main feature is that passing the rigorous nonzero constant shear stress enhanced patch test. To achieve this objective, the following steps have been taken. The first step concerns the choice of the variational framework with the adoption of complementary energy principle. Then boundary displacement interpolation function is established based on the new arbitrary-order Timoshenko beam function. Since the choice of the stress approximation is a crucial issue in developing reliable hybrid finite element, selecting a suitable stress approximation which satisfies the plate equilibrium equations is not trivial. In order to improve the performance of the constructed element, a refined mass matrix for calculation of the natural frequency and a refined geometric stiffness matrix for buckling analysis are developed by using refined element method [24–26].

2. A Brief Introduction of the Higher-Order Hybrid Stress Quadrilateral Mindlin Plate Bending Element

2.1. Fundamental Equations of Mindlin Plate. Consider a plate referred to as a Cartesian coordinate frame (o, x, y, z), with the origin o on the mid-surface Ω and the z-axis in the thickness direction, $-h/2 \le z \le h/2$, where h is the plate thickness. Let $\partial\Omega$ be the boundary of Ω. The Reissner-Mindlin theory, that is, the first-order shear deformable theory, is employed. Thus it is assumed that

$$\begin{aligned} u(x, y, z) &= z\theta_y, \\ v(x, y, z) &= -z\theta_x, \\ w(x, y, z) &= w(x, y), \end{aligned} \tag{1}$$

where u, v, w are displacements along the x-, y-, and z-axes, respectively, θ_x, θ_y are the rotations of the transverse normal about the x- and y-axes, and w is the transverse displacement field.

The geometric equations can be written as follows:

$$\begin{aligned} \boldsymbol{\chi} &= \mathbf{B}_b\boldsymbol{\theta}, \\ \boldsymbol{\gamma} &= \mathbf{B}_s w + \widehat{\mathbf{I}}\boldsymbol{\theta}, \end{aligned} \tag{2}$$

where $\boldsymbol{\theta}$, $\boldsymbol{\chi}$, and $\boldsymbol{\gamma}$ are, respectively, the rotations, the curvatures, and the shear strains:

$$\begin{aligned} \boldsymbol{\theta} &= \begin{bmatrix} \theta_x \\ \theta_y \end{bmatrix}, \\ \boldsymbol{\chi} &= \begin{bmatrix} \chi_x \\ \chi_y \\ \chi_{xy} \end{bmatrix}, \\ \boldsymbol{\gamma} &= \begin{bmatrix} \gamma_{xz} \\ \gamma_{yz} \end{bmatrix}, \end{aligned} \tag{3}$$

and operators $\mathbf{B}_b$, $\mathbf{B}_s$ and $\widehat{\mathbf{I}}$ are given by the following:

$$\mathbf{B}_b = \begin{bmatrix} 0 & \dfrac{\partial}{\partial x} \\ \dfrac{-\partial}{\partial y} & 0 \\ \dfrac{-\partial}{\partial x} & \dfrac{\partial}{\partial y} \end{bmatrix},$$
$$\mathbf{B}_s = \begin{bmatrix} \dfrac{\partial}{\partial x} \\ \dfrac{\partial}{\partial y} \end{bmatrix}, \tag{4}$$
$$\widehat{\mathbf{I}} = \begin{bmatrix} 0 & 1 \\ -1 & 0 \end{bmatrix}.$$

The equilibrium equations can be obtained from the strain energy in the following form:

$$-\mathbf{B}_b^T\mathbf{M} + \widehat{\mathbf{I}}^T\mathbf{S} = \mathbf{0},$$
$$\mathbf{B}_s^T\mathbf{S} = \mathbf{0}, \tag{5}$$

where vectors $\mathbf{M}$ and $\mathbf{S}$ are, respectively, the moment and shear resultants:

$$\mathbf{M} = \begin{bmatrix} M_x \\ M_y \\ M_{xy} \end{bmatrix},$$
$$\mathbf{S} = \begin{bmatrix} S_x \\ S_y \end{bmatrix}. \tag{6}$$

The boundary forces can be written as follows:

$$\mathbf{T} = \mathbf{R}\begin{bmatrix} \mathbf{M} \\ \mathbf{S} \end{bmatrix},$$
$$\mathbf{R} = \begin{bmatrix} 0 & -\sin\alpha & -\cos\alpha & 0 & 0 \\ \cos\alpha & 0 & \sin\alpha & 0 & 0 \\ 0 & 0 & 0 & \cos\alpha & \sin\alpha \end{bmatrix}, \tag{7}$$

where α is the angle between the normal of edge and the local x-axis of element.

For a linearly elastic material, the constitutive equations can be written as follows:

$$\mathbf{M} = \mathbf{D}_b\boldsymbol{\chi},$$
$$\mathbf{S} = \mathbf{D}_s\boldsymbol{\gamma}, \tag{8}$$

where $\mathbf{D}_b$ and $\mathbf{D}_s$ are the elasticity matrices of bending and transverse shear moduli. In the isotropic case, the elasticity matrices specialize as

$$\mathbf{D}_b = \frac{Eh^3}{12\left(1-\mu^2\right)}\begin{bmatrix} 1 & \mu & 0 \\ \mu & 1 & 0 \\ 0 & 0 & \dfrac{1-\mu}{2} \end{bmatrix},$$
$$\mathbf{D}_s = \kappa Gh\begin{bmatrix} 1 & 0 \\ 0 & 1 \end{bmatrix}, \tag{9}$$

where E is Young's modulus, G the shear modulus, μ Poisson's ration, and $\kappa = 5/6$ a correction factor to account for nonuniform distribution of shear stresses through the thickness.

2.2. Hybrid Stress Formulation. Based on a modified complementary energy principle, the assumed stress hybrid formulation pioneered by Pian [28, 29] can be used to avoid the difficulty of forming the displacement field interpolation functions, in particular, after the work of Malkus and Hughes [30] on the equivalence between reduced integration displacements and mixed/hybrid stress models. This kind of approach based on hybrid stress element method became very useful in recent years [31–36]. A good number of effective elements which are free from shear locking have been developed by authors such as Tong [37], Bathe and Dvorkin [38], Ayad et al. [39], Brasile [40], and Li et al. [22, 23]. The higher-order hybrid stress quadrilateral Mindlin plate bending element QH8 is based on complementary energy principle. The complementary energy principle can be written as

$$\Pi_e = \int_{\Omega_e}\frac{1}{2}\boldsymbol{\sigma}^T\mathbf{D}^{-1}\boldsymbol{\sigma}\,d\Omega - \int_{\partial\Omega_e}\mathbf{T}^T\overline{\mathbf{u}}\,dS, \tag{10}$$

where $\boldsymbol{\sigma}$ is the stress vector, $\mathbf{D}$ is the elasticity matrices, $\mathbf{T}$ is the vector of boundary force, $\overline{\mathbf{u}} = [\widetilde{w}\ \ \widetilde{\theta}_x\ \ \widetilde{\theta}_y]^T$ is the boundary displacement vector, $\widetilde{w}$ is the transverse displacement, and $\widetilde{\theta}_x$, $\widetilde{\theta}_y$ are the rotations of the transverse normal about the x- and y-axes.

The approximation for stress and boundary displacements can now be incorporated in the functional. The stress field is described in the interior of the element as follows:

$$\left[M_x\ \ M_y\ \ M_{xy}\ \ S_x\ \ S_y\right]^T = \mathbf{P}\boldsymbol{\beta}, \tag{11}$$

where $\mathbf{P}$ is matrix of stress interpolation functions and $\boldsymbol{\beta}$ is the unknown stress parameters.

The boundary force $\mathbf{T}$ can be represented as follows:

$$\mathbf{T} = \mathbf{RP}\boldsymbol{\beta}, \tag{12}$$

where $\mathbf{R}$ is the combination of direction cosine for the boundary normal.

The boundary displacement field is described by

$$\overline{\mathbf{u}} = \left[\widetilde{w}\ \ \widetilde{\theta}_x\ \ \widetilde{\theta}_y\right]^T = \mathbf{Lq}, \tag{13}$$

where **L** are interpolation functions and **q** is nodal displacement parameters.

Substituting the stress equation (11), boundary force equation (12), and displacement approximations equation (13) into the functional (10),

$$\Pi_e = \frac{1}{2}\boldsymbol{\beta}^T\mathbf{H}\boldsymbol{\beta} - \boldsymbol{\beta}^T\mathbf{G}\mathbf{q}, \tag{14}$$

where

$$\begin{aligned}\mathbf{H} &= \int_{\Omega_e}\mathbf{P}^T\mathbf{D}^{-1}\mathbf{P}\,d\Omega\\ \mathbf{G} &= \int_{\partial\Omega_e}(\mathbf{R}\mathbf{P})^T\,\mathbf{L}\,dS.\end{aligned} \tag{15}$$

The form of (15) is directly amenable to numerical integration (i.e., Gauss quadrature).

Then the internal strain energy can be expressed as follows:

$$U = \int_{\Omega_e}\frac{1}{2}\boldsymbol{\sigma}^T\mathbf{D}^{-1}\boldsymbol{\sigma}\,d\Omega = \frac{1}{2}\boldsymbol{\beta}^T\mathbf{H}\boldsymbol{\beta}. \tag{16}$$

By means of $\partial\Pi_e/\partial\boldsymbol{\beta}$, we obtained

$$\mathbf{H}\boldsymbol{\beta} = \mathbf{G}\mathbf{q}. \tag{17}$$

Consequently,

$$\boldsymbol{\beta} = \mathbf{H}^{-1}\mathbf{G}\mathbf{q}. \tag{18}$$

Substitution of $\boldsymbol{\beta}$ in (16), the internal strain energy reduces to

$$U = \frac{1}{2}\mathbf{q}^T\mathbf{G}^T\mathbf{H}^{-1}\mathbf{G}\mathbf{q}. \tag{19}$$

Compared with $U = (1/2)\mathbf{q}^T\mathbf{K}\mathbf{q}$, the element stiffness matrix can be taken as

$$\mathbf{K} = \mathbf{G}^T\mathbf{H}^{-1}\mathbf{G}. \tag{20}$$

The solution of the system yields the unknown nodal displacement **q**. After **q** is determined, element stress or internal forces can be recovered by use of (18) and (11). Thus

$$\boldsymbol{\sigma} = \mathbf{P}\mathbf{H}^{-1}\mathbf{G}\mathbf{q}. \tag{21}$$

2.3. The Displacement Interpolation Function of QH8 Element. Euler-Bernoulli beam function has been successfully employed in the construction of refined thin plate elements. It is well-known that when constructing Mindlin plate element, both thick and thin plates should be taken into account, and it is necessary to eliminate shear-locking phenomenon. To seek out such element displacement function is definitely very difficult. Note that a closed form solution for both thick and thin beams exists in the form of the Timoshenko beam function, and it is possible to use it to derive more efficient Mindlin plate elements [41]. However, the use of Timoshenko beam function is capable of solving the problem of shear locking; it cannot solve the problem of passing the nonzero constant shear patch test. This problem has not resolved for many years. In 2011, Jelenić and Papa [21] presented a new arbitrary-order Timoshenko beam function as follows:

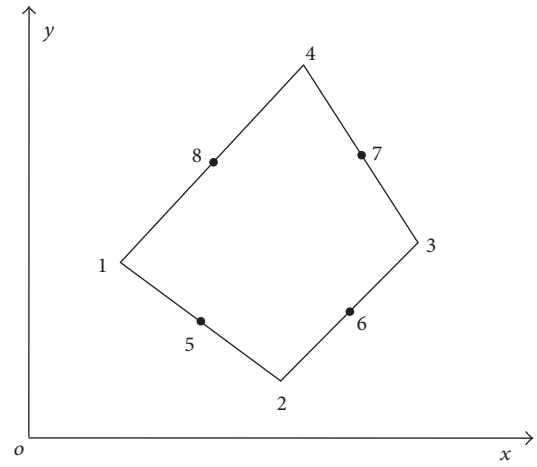

Figure 1: Eight-node quadrilateral plate element.

$$\begin{aligned}w &= \sum_{i=1}^{n} I_i w_i - \frac{L}{n}\prod_{j=1}^{n} N_j \sum_{i=1}^{n}(-1)^{i-1}\binom{n-1}{i-1}\theta_i\\ \theta &= \sum_{i=1}^{n} I_i\theta_i,\end{aligned} \tag{22}$$

where L is the beam length, w_i and θ_i are the values of the displacements and the rotations at the n nodes equidistantly spaced between the beam ends, I_i are the standard Lagrange polynomials of order $n-1$, and $N_j = x/L$ for $j = 1$ and $N_j = 1-(n-1)/(j-1)(x/L)$ otherwise, in which x is the coordinate along the beam.

An 8-node quadrilateral element was designed as given in Figure 1. If any quadrilateral side is taken as a beam element, take the 1-2 boundary as example and the deflection $\widetilde{w}$ and rotations $\widetilde{\theta}_x, \widetilde{\theta}_y$ can be derived as follows:

$$\begin{aligned}\widetilde{w} &= I_1 w_1 + I_2 w_2 + I_5 w_5 - I_0 L\left(-\theta_{n,1} + 2\theta_{n,5} - \theta_{n,2}\right)\\ &= I_1 w_1 + I_2 w_2 + I_5 w_5 - I_0\left[\left(-\theta_{x,1} + 2\theta_{x,5} - \theta_{x,2}\right)b\right.\\ &\quad\left.+\left(-\theta_{y,1} + 2\theta_{y,5} - \theta_{y,2}\right)a\right]\\ \widetilde{\theta}_x &= I_1\theta_{x,1} + I_2\theta_{x,2} + I_5\theta_{x,5}\\ \widetilde{\theta}_y &= I_1\theta_{y,1} + I_2\theta_{y,2} + I_5\theta_{y,5},\end{aligned} \tag{23}$$

where $I_1 = L_1(2L_1-1)$, $I_2 = L_2(2L_2-1)$, $I_5 = 4L_1L_2$, $I_0 = (1/3)L_1L_2(L_2-L_1)$, $L_1 = 1-s/L$, $L_2 = s/L$, L is the length of 1-2 boundary and s is the coordinate along the 1-2 edge.

The displacement components $\overline{\mathbf{u}}$ along the 1-2 boundary was given as follows:

$$\overline{\mathbf{u}}_{\mathbf{1\text{-}2}} = \left[\widetilde{w} \;\; \widetilde{\theta}_x \;\; \widetilde{\theta}_y\right]^T = \mathbf{L}_{1\text{-}2}\mathbf{q}_{1\text{-}2}, \tag{24}$$

where

$$\mathbf{L}_{1\text{-}2} = \begin{bmatrix} I_1 & I_0 b & I_0 a & I_2 & I_0 b & I_0 a & I_5 & -2I_0 b & -2I_0 a \\ 0 & I_1 & 0 & 0 & I_2 & 0 & 0 & I_5 & 0 \\ 0 & 0 & I_1 & 0 & 0 & I_2 & 0 & 0 & I_5 \end{bmatrix} \tag{25}$$

and $\mathbf{q}_{1\text{-}2} = [\mathbf{q}_1 \;\; \mathbf{q}_2 \;\; \mathbf{q}_5]^T$, $\mathbf{q}_i = [w_i \;\; \theta_{xi} \;\; \theta_{yi}]^T$ $(i = 1, 2, 5)$.

2.4. Assumed Stresses. In this section, a strategy to select the stress approximation in a rational way is presented. In practice, initial polynomials are usually assumed for the stress after which the equilibrium equations are applied to these polynomials yielding relations between the β's and ultimately the final form of $\mathbf{P}$. The number of stress parameters, which is the number of columns in $\mathbf{P}$, must be at least equal to the number of degrees of freedom of the element less the number of degrees of freedom necessary to prevent rigid body motion.

In a series of studies of hybrid element, there is a general consensus on the selection of $\boldsymbol{\beta}$ parameter that is $N(\boldsymbol{\beta}) \geq n_d - n_r$, while the optimal selection is $N(\boldsymbol{\beta}) = n_d - n_r$, n_d, n_r being the degrees of freedom of the element and the number of allowed rigid body motions, respectively. The element has 24 DOF; therefore, a stress field with at least 21 parameters is needed to describe the stress field and without spurious zero-energy modes. Numerical results show that the stiffness matrix has spurious zero-energy modes and converges slowly when $N(\boldsymbol{\beta}) = 21$. The finds that gradually increasing the number of $\{\beta_i\}$ until $N(\boldsymbol{\beta}) = 28$, there is a proper rank for the stiffness matrix and the absence of spurious zero-energy modes. Moreover, the calculation results are accurate and converged faster. And they are better if the number of $\{\beta_i\}$ reaches $N_b = 39$ (complete quartic polynomial). Numerical experimentations [23] indicate that this 39-parameter selection of stress field is somewhat more accurate and has no spurious zero-energy modes. For this reason, 39β are chosen as the assumed stress field.

The stress field is described in the interior of the element as follows:

$$\left[M_x \;\; M_y \;\; M_{xy} \;\; Q_x \;\; Q_y\right]^T = \mathbf{P}\boldsymbol{\beta}, \tag{26}$$

where $\mathbf{P}$ is matrix of stress interpolation functions as shown in Table 1, and $\boldsymbol{\beta}$ is the stress parameters.

From (12), the boundary force $\mathbf{T}$ can be expressed as

$$\mathbf{T} = \mathbf{RP}\boldsymbol{\beta}. \tag{27}$$

Then, along the boundary 1-2, $\mathbf{G}$ can be obtained:

$$\mathbf{G}_{12} = \int_{\partial\Omega(1\text{-}2)} (\mathbf{RP})^T \mathbf{L}_{1\text{-}2}\, ds. \tag{28}$$

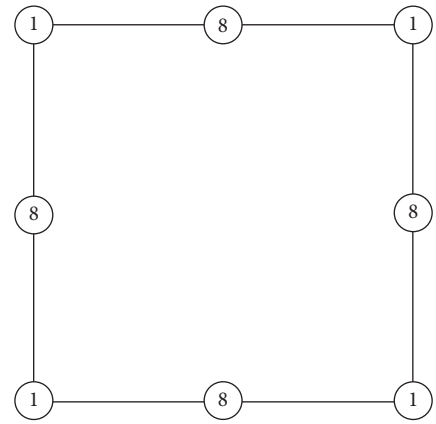

Figure 2: Mass lumping at the nodes.

Similarly, along the other boundaries, $\mathbf{G}_{23}$, $\mathbf{G}_{34}$, $\mathbf{G}_{41}$ can also be obtained by cyclic permutation.

3. The Refined Mass Matrix and Refined Geometric Stiffness Matrix for Vibration and Buckling Analysis of Plates

A refined method has been developed by the authors [24, 25], and the method has been applied to develop 12-DOF [15], 9-DOF [16], and 5-DOF [49] Mindlin elements and so forth. This method is applied here to formulate QH8-RCV with a mass matrix called refined mass matrix for calculation of the natural frequency and in the same way QH8-R with a refined geometric stiffness matrix for buckling analysis.

3.1. Free Vibration Analysis. It is well-known that the equation of free vibration can be expressed as follows:

$$\left(\mathbf{K} - \omega^2\mathbf{M}\right)\boldsymbol{\Phi} = \mathbf{0}, \tag{29}$$

where $\mathbf{K}$ is the global stiffness matrix, $\mathbf{M}$ is the global mass matrix, $\boldsymbol{\Phi}$ is the mode shapes, and ω is the natural frequencies.

The major complication of the standard eigenvalue problem introduced by the finite element method is the mass matrix $\mathbf{M}$. Two types of the mass matrix are of interest: lumped mass matrix and consistent mass matrix.

3.1.1. The Lumped Mass Matrix. To use the diagonal elements of the consistent mass matrix and form a diagonal matrix by scaling these entries so that the total mass of the element is conserved, the method listed by Hinton et al. [50] produces excellent results. For the cases of eight-node elements, the method leads to the lumping schemes shown in Figure 2. The figures at each node show the proportion of the total mass at that node. For convenience, the total mass has been chosen to be 36. Therefore the following lumped mass matrix will be used to calculate the natural frequencies of plates:

Table 1: Assumed stress function.

i	M_x	M_y	M_{xy}	Q_x	Q_y
1	1	0	0	0	0
2	0	1	0	0	0
3	0	0	1	0	0
4	x	0	0	1	0
5	y	0	0	0	0
6	0	x	0	0	0
7	0	y	0	0	1
8	0	0	x	0	1
9	0	0	y	1	0
10	x^2	0	$-xy$	x	$-y$
11	xy	0	0	y	0
12	y^2	0	0	0	0
13	0	x^2	0	0	0
14	0	xy	0	0	x
15	0	y^2	$-xy$	$-x$	y
16	0	0	x^2	0	$2x$
17	0	0	y^2	$2y$	0
18	x^3	0	$-1.5x^2y$	$1.5x^2$	$-3xy$
19	x^2y	0	$-0.5xy^2$	xy	$-0.5y^2$
20	xy^2	0	0	y^2	0
21	y^3	0	0	0	0
22	0	x^3	0	0	0
23	0	x^2y	0	0	x^2
24	0	xy^2	$-0.5x^2y$	$-0.5x^2$	xy
25	0	y^3	$-1.5xy^2$	$-3xy$	$1.5y^2$
26	0	0	x^3	0	$3x^2$
27	0	0	y^3	$3y^2$	0
28	x^4	$-6x^2y^2$	0	$4x^3$	$-12x^2y$
29	x^3y	0	$-0.75x^2y^2$	$1.5x^2y$	$-1.5xy^2$
30	xy^3	0	0	y^3	0
31	y^4	0	0	0	0
32	0	x^4	0	0	0
33	0	x^3y	0	0	x^3
34	0	xy^3	$-0.75x^2y^2$	$-1.5x^2y$	$1.5xy^2$
35	$-6x^2y^2$	y^4	0	$-12xy^2$	$4y^3$
36	0	0	x^4	0	$4x^3$
37	0	$-3x^2y^2$	x^3y	x^3	$-3x^2y$
38	$-3x^2y^2$	0	xy^3	$-3xy^2$	y^3
39	0	0	y^4	$4y^3$	0

$$\mathbf{M}^e_{\text{lumped}} = \frac{m_e}{36}\,\text{diag}\left[1\ \ 0\ \ 0\ \ 1\ \ 0\ \ 0\ \ 1\ \ 0\ \ 0\ \ 1\ \ 0\ \ 0\ \ 8\ \ 0\ \ 0\ \ 8\ \ 0\ \ 0\ \ 8\ \ 0\ \ 0\ \ 8\ \ 0\ \ 0\right], \tag{30}$$

where m_e is the element mass.

3.1.2. The Refined Consistent Mass Matrix. In order to improve the accuracy of the natural frequencies, the refined mass matrix has been used in the eigenproblem of the finite element method. We can give herein a new approach for improving the consistent mass matrix which can be obtained from a combination of the element displacement interpolations.

As for free vibration analysis, 8-node shape function is used to interpolate the displacement function components w, θ_x, θ_y as

$$\begin{aligned} w &= \sum_{i=1}^{8} N_i w_i, \\ \theta_x &= \sum_{i=1}^{8} N_i \theta_{xi}, \\ \theta_y &= \sum_{i=1}^{8} N_i \theta_{yi}, \end{aligned} \tag{31}$$

where

$$\begin{aligned} N_i &= \frac{1}{4}\left(1+\xi_i\xi\right)\left(1+\eta_i\eta\right)\left(\xi_i\xi+\eta_i\eta-1\right), \\ &\qquad\qquad i = 1,2,3,4 \\ N_i &= \frac{1}{2}\left(1-\xi^2\right)\left(1+\eta_i\eta\right), \quad i = 5,7 \\ N_i &= \frac{1}{2}\left(1-\eta^2\right)\left(1+\xi_i\xi\right), \quad i = 6,8. \end{aligned} \tag{32}$$

Another 4-node shape functions are used to interpolate the deflection part of displacement function as

$$w_b = \sum_{i=1}^{4} \overline{N}_i w_i, \tag{33}$$

where

$$\overline{N}_i = \frac{1}{4}\left(1+\xi_i\xi\right)\left(1+\eta_i\eta\right), \quad i = 1,2,3,4. \tag{34}$$

So the new deflection function part w^* can be described as

$$w^* = w + \alpha\left(w - w_b\right), \tag{35}$$

where α is an adjustable constant which is used to improve the accuracy of the vibration analysis.

Based on (31), (33), and (35), the shape function of refined consistent mass matrix is of the following form:

$$\left[w^* \ \ \theta_x \ \ \theta_y\right]^T = \left[w + \alpha\left(w - w_b\right) \ \ \theta_x \ \ \theta_y\right]^T = \mathbf{Nq} \tag{36}$$

and the element consistent mass matrix $\mathbf{M}^e_c$ can be expressed as

$$\mathbf{M}^e_c = \iint_\Omega \mathbf{N}^T\mathbf{m}\mathbf{N}\,dx\,dy, \tag{37}$$

where $\mathbf{m}$ is the matrix containing the mass density of the material ρ and thickness t as follows:

$$\mathbf{m} = \rho\begin{pmatrix} t & 0 & 0 \\ 0 & \dfrac{t^3}{12} & 0 \\ 0 & 0 & \dfrac{t^3}{12} \end{pmatrix}. \tag{38}$$

3.2. Buckling Analysis Problem and Refined Geometric Stiffness Matrix. Consider a plate under an initial stress which may induce instability. Similar to the free vibration problem of plate, the equation of stability analysis can be expressed as

$$\left(\mathbf{K} - \lambda\mathbf{K}_G\right)\mathbf{\Phi} = 0, \tag{39}$$

where $\mathbf{K}$ is the global stiffness matrix, $\mathbf{K}_G$ is the geometric stiffness matrix of the whole structure, λ is the critical load, and $\mathbf{\Phi}$ is the mode shape of buckling. The element geometric stiffness matrix $\mathbf{K}^e_G$ can be written as

$$\mathbf{K}^e_G = \mathbf{K}^e_{G1} + \mathbf{K}^e_{G2} + \mathbf{K}^e_{G3}, \tag{40}$$

where the terms of (40) are

$$\begin{aligned} \mathbf{K}^e_{G1} &= t\int_{\Omega_e}\begin{bmatrix}\dfrac{\partial w}{\partial x} & \dfrac{\partial w}{\partial y}\end{bmatrix}\left(\sigma^0\right)^T\begin{bmatrix}\dfrac{\partial w}{\partial x} \\ \dfrac{\partial w}{\partial y}\end{bmatrix}dx\,dy \\ \mathbf{K}^e_{G2} &= \frac{t^3}{12}\int_{\Omega_e}\begin{bmatrix}\dfrac{\partial \theta_x}{\partial x} & \dfrac{\partial \theta_x}{\partial y}\end{bmatrix}\left(\sigma^0\right)^T\begin{bmatrix}\dfrac{\partial \theta_x}{\partial x} \\ \dfrac{\partial \theta_x}{\partial y}\end{bmatrix}dx\,dy \\ \mathbf{K}^e_{G3} &= \frac{t^3}{12}\int_{\Omega_e}\begin{bmatrix}\dfrac{\partial \theta_y}{\partial x} & \dfrac{\partial \theta_y}{\partial y}\end{bmatrix}\left(\sigma^0\right)^T\begin{bmatrix}\dfrac{\partial \theta_y}{\partial x} \\ \dfrac{\partial \theta_y}{\partial y}\end{bmatrix}dx\,dy \end{aligned} \tag{41}$$

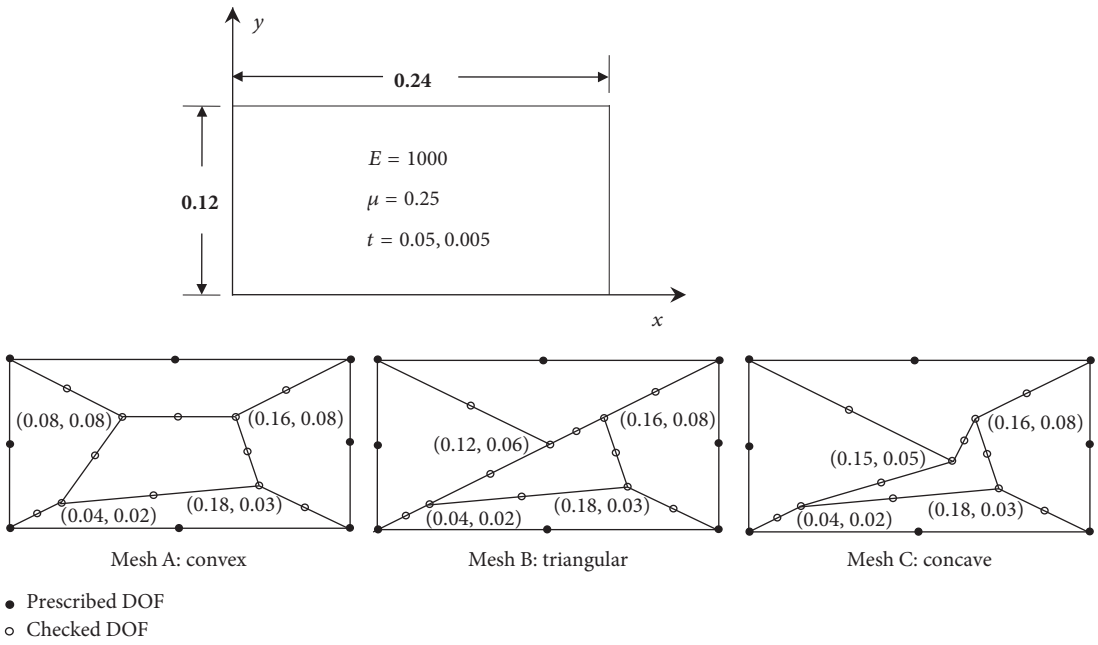

Figure 3: Constant stress patch test.

and vector $\sigma^0 = \begin{bmatrix} \sigma_x^0 & \tau_{xy}^0 \\ \tau_{xy}^0 & \sigma_y^0 \end{bmatrix}$ stands for the initial stress of plate, σ_x^0, σ_y^0 are unit tractions in the direction of x and y, and τ_{xy}^0 is the unit shear stress.

Similarly, we can obtain the refined geometric stiffness matrix from the following relation:

$$\begin{Bmatrix} \dfrac{\partial \overline{w}}{\partial x} \\ \dfrac{\partial \overline{w}}{\partial y} \end{Bmatrix} = \begin{Bmatrix} \dfrac{\partial w}{\partial x} \\ \dfrac{\partial w}{\partial y} \end{Bmatrix} + \alpha_0 \left(\begin{Bmatrix} \dfrac{\partial w}{\partial x} \\ \dfrac{\partial w}{\partial y} \end{Bmatrix} - \begin{Bmatrix} \theta_y \\ -\theta_x \end{Bmatrix} \right) + \alpha_0 \left(\begin{Bmatrix} \dfrac{\partial w}{\partial x} \\ \dfrac{\partial w}{\partial y} \end{Bmatrix} - \begin{Bmatrix} \dfrac{\partial w_b}{\partial x} \\ \dfrac{\partial w_b}{\partial y} \end{Bmatrix} \right), \tag{42}$$

where α_0 is an adjustable constant used to improve the accuracy of the stability analysis, the displacement interpolation functions w, θ_x, θ_y are the same as 8-node shape function (31), and w_b is in terms of (33).

Based on (42), we only modify the interpolation function w and geometric stiffness matrix part $\mathbf{K}_{G1}^e$ as

$$\overline{\mathbf{K}}_{G1}^e = t \int_{\Omega_e} \begin{bmatrix} \dfrac{\partial \overline{w}}{\partial x} & \dfrac{\partial \overline{w}}{\partial y} \end{bmatrix} \left(\sigma^0\right)^T \begin{bmatrix} \dfrac{\partial \overline{w}}{\partial x} \\ \dfrac{\partial \overline{w}}{\partial y} \end{bmatrix} dx\, dy. \tag{43}$$

The refined geometric stiffness matrix can be written as

$$\overline{\mathbf{K}}_G^e = \overline{\mathbf{K}}_{G1}^e + \mathbf{K}_{G2}^e + \mathbf{K}_{G3}^e. \tag{44}$$

4. Numerical Examples

To investigate the accuracy and reliability of the proposed QH8 element for free vibration analysis and buckling analysis, several numerical examples with different geometry and boundary condition are calculated in this section. For convenience, the boundaries of plates are denoted as follows: clamped supported (C), hard-type simply supported (S), soft-type simply supported (S*), and free (F), so a boundary condition can be written as CCCC, SSSS, CFFF, SCSC, SFSF, and so on for a rectangular plate. For example, the symbol, SFCF, represents simply supported edge along $x = 0$, a free edge along $y = 0$, a clamped edge along $x = a$, and a free edge along $y = b$.

4.1. Patch Test: Consistency Assessment. Consistency of the developed elements is tested for the constant strain and stress states on the patch example with five elements, covering a rectangular domain of a plate as shown in Figure 3. The size of the domain is 0.24×0.12. The mechanical properties of the plate are chosen as $E = 10^3$, $\mu = 0.25$, $\kappa = 5/6$.

For zero shear deformation patch test, the test function [20, 23] can be written as follows:

$$\begin{aligned} w &= a_0 + a_1 x + a_2 y + a_3 x^2 + a_4 xy + a_5 y^2 \\ \theta_x &= a_2 + a_4 x + 2a_5 y \\ \theta_y &= -a_1 - 2a_3 x - a_4 y. \end{aligned} \tag{45}$$

Table 2: Numerical results of constant bending patch test (at node (0.04, 0.02)).

	w	θ_x	θ_y	M_x	M_y	M_{xy}	S_x	S_y
				$t = 0.05$				
Mesh A	1.1528	3.440	−2.420	−0.12222	−0.15556	−0.041667	0	0
Mesh B	1.1528	3.440	−2.420	−0.12222	−0.15556	−0.041667	0	0
Mesh C	1.1528	3.440	−2.420	−0.12222	−0.15556	−0.041667	0	0
Exact	1.1528	3.440	−2.420	−0.12222	−0.15556	−0.041667	0	0
				$t = 0.005$				
Mesh A	1.1528	3.440	−2.420	−0.0001222	−0.0001556	−0.000041667	0	0
Mesh B	1.1528	3.440	−2.420	−0.0001222	−0.0001556	−0.000041667	0	0
Mesh C	1.1528	3.440	−2.420	−0.0001222	−0.0001556	−0.000041667	0	0
Exact	1.1528	3.440	−2.420	−0.0001222	−0.0001556	−0.000041667	0	0

Table 3: Numerical results of nonzero constant shear stress patch test (at node (0.04, 0.02)).

	w	θ_x	θ_y	M_x	M_y	M_{xy}	S_x	S_y
				$t = 0.05$				
Mesh A	1.1537	3.529867	−2.51	−0.156667	−0.196667	−0.053	−0.66667	−0.84444
Mesh B	1.1537	3.529867	−2.51	−0.156667	−0.196667	−0.053	−0.66667	−0.84444
Mesh C	1.1537	3.529867	−2.51	−0.156667	−0.196667	−0.053	−0.66667	−0.84444
Exact	1.1537	3.529867	−2.51	−0.156667	−0.196667	−0.053	−0.66667	−0.84444
				$t = 0.005$				
Mesh A	1.1537	3.479707	−2.4704	−0.0001567	−0.0001967	−0.000053	−0.00067	−0.000844
Mesh B	1.1537	3.479707	−2.4704	−0.0001567	−0.0001967	−0.000053	−0.00067	−0.000844
Mesh C	1.1537	3.479707	−2.4704	−0.0001567	−0.0001967	−0.000053	−0.00067	−0.000844
Exact	1.1537	3.479707	−2.4704	−0.0001567	−0.0001967	−0.000053	−0.00067	−0.000844

For nonzero shear deformation patch test, the test function can be expressed as follows:

$$\begin{aligned} w &= a_0 + a_1 x + a_2 y + a_3 x^2 + a_4 xy + a_5 y^2 + a_6 x^3 \\ &\quad + a_7 x^2 y + a_8 x y^2 + a_9 y^3 \\ \theta_x &= \frac{h^2}{3k(1-\mu)}(a_7 + 3a_9) + a_2 + a_4 x + 2a_5 y + a_7 x^2 \\ &\quad + 2a_8 xy + 3a_9 y^2 \\ \theta_y &= -\frac{h^2}{3k(1-\mu)}(3a_6 + a_8) - a_1 - 2a_3 x - a_4 y \\ &\quad - 3a_6 x^2 - 2a_7 xy - a_8 y^2, \end{aligned} \tag{46}$$

where a_i, $(i = 0, \ldots, 9)$ are arbitrary constants. In the present paper, we assume that $a_i = i + 1$.

The mesh of patch test is presented in Figure 3. The displacements at the nodes on the boundaries are imposed according to (45) and (46), given the displacements and rotations at the boundary nodes (8 displacements and 16 rotations), while all the internal nodal displacements and rotations are to be calculated by the finite element solution procedure.

Test results show that the element QH8-39β passes both the constant bending with zero shear stresses S_x, S_y (Table 2) and the strict patch test with nonzero constant shear stresses S_x, S_y (Table 3). No matter the inner element edges are straight or curved, and no matter the shapes of the elements are convex or concave, the exact results of the displacements and stresses at inner node obtained using the present QH8-39β element agree well with the test functions. This demonstrates that the new element passes the strict constant stress patch test, thus ensuring solution convergence.

4.2. Free Vibration Analysis. In this section, we examine the efficiency and the applicability of the 8-node quadrilateral hybrid stress element in analyzing natural frequencies of plates. The proposed 8-node quadrilateral hybrid stress elements with lumped mass matrix (30) and refined consistent mass matrix (37) in vibration analysis are denoted by QH8-LV and QH8-RCV, respectively.

The effects of various slenderness ratios, skew angles, and boundary conditions on the frequencies are also discussed. Unless other stated, the following material parameters are used throughout the paper: Young's modulus $E = 2.0 \times 10^{11}$, Poisson's ratio $\mu = 0.3$, the mass density of the material $\rho = 8000$, and the shear correction factor $\kappa = 5/6$ is taken if not specified otherwise.

Table 4: The six lowest nondimensional frequency parameters of a CCCC thin square plate ($t/L = 0.001$).

Element (α)	Mode sequence number					
	1	2	3	4	5	6
QH8-RCV(−1)	3.6742	7.5726	7.5726	11.2791	13.8025	13.8626
QH8-RCV(−0.5)	3.6602	7.5052	7.5052	11.1242	13.5707	13.6325
QH8-RCV(−0.25)	3.6532	7.4711	7.4711	11.0458	13.4531	13.5157
QH8-RCV(−0.08)	3.6484	7.4478	7.4478	10.9922	13.3726	13.4356
QH8-RCV(0)	3.6461	7.4368	7.4368	10.9669	13.3345	13.3978
QH8-LV	3.6460	7.4363	7.4363	10.9644	13.3318	13.3949
Reference [27]	3.646	7.436	7.436	10.964	13.332	13.395

Table 5: The six lowest nondimensional frequency parameters of a CCCC thick square plate ($t/L = 0.1$).

Element (α)	Mode sequence number					
	1	2	3	4	5	6
QH8-RCV(−1)	3.3118	6.3402	6.3402	8.9003	10.4844	10.5761
QH8-RCV(−0.5)	3.3066	6.3332	6.3332	8.9090	10.5178	10.6160
QH8-RCV(−0.25)	3.3002	6.3038	6.3038	8.8443	10.4237	10.5216
QH8-RCV(−0.08)	3.2943	6.2743	6.2743	8.7752	10.3198	10.4162
QH8-RCV(0)	3.2912	6.2578	6.2578	8.7360	10.2604	10.3558
QH8-LV	3.3181	6.3688	6.3688	8.9622	10.5759	10.6670
Reference [27]	3.292	6.276	6.276	8.792	10.356	10.455

Table 6: The six lowest nondimensional frequency parameters of a SSSS thin square plate ($t/L = 0.001$).

Element (α)	Mode sequence number					
	1	2	3	4	5	6
QH8-RCV(−1)	2.0129	5.0805	5.0805	8.2063	10.3226	10.3226
QH8-RCV(−0.5)	2.0064	5.0403	5.0403	8.1034	10.1616	10.1616
QH8-RCV(−0.25)	2.0032	5.0202	5.0202	8.0522	10.0813	10.0813
QH8-RCV(−0.08)	2.0010	5.0066	5.0066	8.0174	10.0268	10.0268
QH8-RCV(0)	2.0000	5.0002	5.0002	8.0010	10.0012	10.0012
QH8-LV	2.0000	5.0000	5.0000	7.9998	9.9999	9.9999
Reference [27]	2.000	5.000	5.000	8.000	10.000	10.000

In the numerical calculation, the dimensionless solutions of natural frequencies with a multiplier $\pi^2/b^2\sqrt{D/\rho}$ are obtained. b is the width of the edge, $D = Et^3/12(1-\mu^2)$. Unless otherwise specified, the actual computations are done using dimensionless units.

4.2.1. Square Plate. For the hybrid stress element with the lumped mass matrix (QH8-LV) and refined mass matrix (QH8-RCV), the fundamental natural frequencies or free vibration problems of a square plate with different meshes and different boundary conditions are calculated.

The parameter α in (36) for the present element QH8-RCV (8-node hybrid element with refined mass matrix) is determined by comparison using numerical examples. A square plate (the length of the plate a and the width of the plate b: $a/b = 1$) is divided into mesh of 16×16 elements. The thickness-to-width aspect ratios $t/b = 0.001, 0.1$, boundary conditions SSSS, CCCC, and $\alpha = -1, -0.5, -0.25, -0.08, 0$ are chosen. The results of six lowest modes are given in Tables 4–7 and Figure 4, in which the exact solutions can be found in [27]. We advise $\alpha = -0.08$ of the present QH8-RCV(α) for following numerical examples.

The convergence of frequencies results of thin and thick square plates with SSSS and CCCC boundary conditions for QH8-RCV(−0.08) and QH8-LV are shown in Table 8 and Figure 5. The square plate is discretized by $N \times N$ uniform meshes with $N = 4, 8, 16$. The results agree well with [27] when $N = 8, 16$.

Then, natural frequencies analyses are further carried on the thin ($t/b = 0.001$) and thick ($t/b = 0.1$) square plate with the meshes of 16×16 elements and various boundary conditions such as SSFF, SFSF, SCSC, CFFF, CCFF, and CFCF. The results are summarized in Table 9 and agree well with [27]. The six lowest modes of clamped and simply supported (CCCC, SSSS) thin square plate obtained by the QH8-RCV are also investigated and plotted in Figure 6.

Table 7: The six lowest nondimensional frequency parameters of a SSSS thick square plate ($t/L = 0.1$).

Element (α)	Mode sequence number					
	1	2	3	4	5	6
QH8-RCV(−1)	1.9424	4.6599	4.6599	7.1742	8.7513	8.7513
QH8-RCV(−0.5)	1.9376	4.6420	4.6420	7.1505	8.7325	8.7325
QH8-RCV(−0.25)	1.9345	4.6229	4.6229	7.1032	8.6600	8.6600
QH8-RCV(−0.08)	1.9321	4.6062	4.6062	7.0581	8.5881	8.5881
QH8-RCV(0)	1.9308	4.5973	4.5973	7.0335	8.5482	8.5482
QH8-LV	1.9457	4.6784	4.6784	7.2173	8.8157	8.8157
Reference [27]	1.931	4.605	4.605	7.064	8.605	8.605

Table 8: Convergence of six lowest nondimensional frequency parameters ($t/h = 0.001$, 0.1 and SSSS, CCCC).

t/L	Boundary	Mesh	Mode sequence number					
			1	2	3	4	5	6
(a) QH8 with modified consistent mass matrix (QH8-RCV, $\alpha = -0.08$)								
0.001	SSSS	4 × 4	2.0208	5.1600	5.1600	8.5457	10.7782	10.7782
		8 × 8	2.0044	5.0290	5.0290	8.0832	10.1251	10.1251
		16 × 16	2.0010	5.0066	5.0066	8.0174	10.0268	10.0268
		Ref. sol	2.000	5.000	5.000	8.000	10.000	10.000
	CCCC	4 × 4	3.6986	7.7478	7.7478	11.8207	14.7803	14.9043
		8 × 8	3.6563	7.4895	7.4895	11.1031	13.5317	13.5943
		16 × 16	3.6484	7.4478	7.4478	10.9922	13.3726	13.4356
		Ref. sol	3.646	7.436	7.436	10.964	13.332	13.395
0.1	SSSS	4 × 4	1.9440	4.6822	4.6822	7.3572	8.9607	8.9607
		8 × 8	1.9335	4.6062	4.6062	7.0516	8.5663	8.5663
		16 × 16	1.9321	4.6062	4.6062	7.0581	8.5881	8.5881
		Ref. sol	1.931	4.605	4.605	7.064	8.605	8.605
	CCCC	4 × 4	3.3008	6.3401	6.3401	9.0667	10.7861	10.8677
		8 × 8	3.2925	6.2555	6.2555	8.7327	10.2492	10.3400
		16 × 16	3.2943	6.2743	6.2743	8.7752	10.3198	10.4162
		Ref. sol	3.292	6.276	6.276	8.792	10.356	10.455
(b) QH8 with lumped mass matrix (QH8-LV)								
0.001	SSSS	4 × 4	1.9997	4.9970	4.9970	7.9691	9.9694	9.9694
		8 × 8	2.0000	4.9999	4.9999	7.9986	10.0001	10.0001
		16 × 16	2.0000	5.0000	5.0000	7.9998	9.9999	9.9999
		Ref. sol	2.000	5.000	5.000	8.000	10.000	10.000
	CCCC	4 × 4	3.6452	7.4121	7.4121	10.8713	12.9885	13.0468
		8 × 8	3.6461	7.4365	7.4365	10.9637	13.3312	13.3935
		16 × 16	3.6460	7.4363	7.4363	10.9644	13.3318	13.3949
		Ref. sol	3.646	7.436	7.436	10.964	13.332	13.395
0.1	SSSS	4 × 4	1.9427	4.6385	4.6385	7.0569	8.5511	8.5511
		8 × 8	1.9452	4.6710	4.6710	7.1895	8.7670	8.7670
		16 × 16	1.9457	4.6784	4.6784	7.2173	8.8157	8.8157
		Ref. sol	1.931	4.605	4.605	7.064	8.605	8.605
	CCCC	4 × 4	3.3019	6.2524	6.2524	8.6322	10.0169	10.0917
		8 × 8	3.3155	6.3496	6.3496	8.9075	10.4886	10.5773
		16 × 16	3.3181	6.3688	6.3688	8.9622	10.5759	10.6670
		Ref. sol	3.292	6.276	6.276	8.792	10.356	10.455

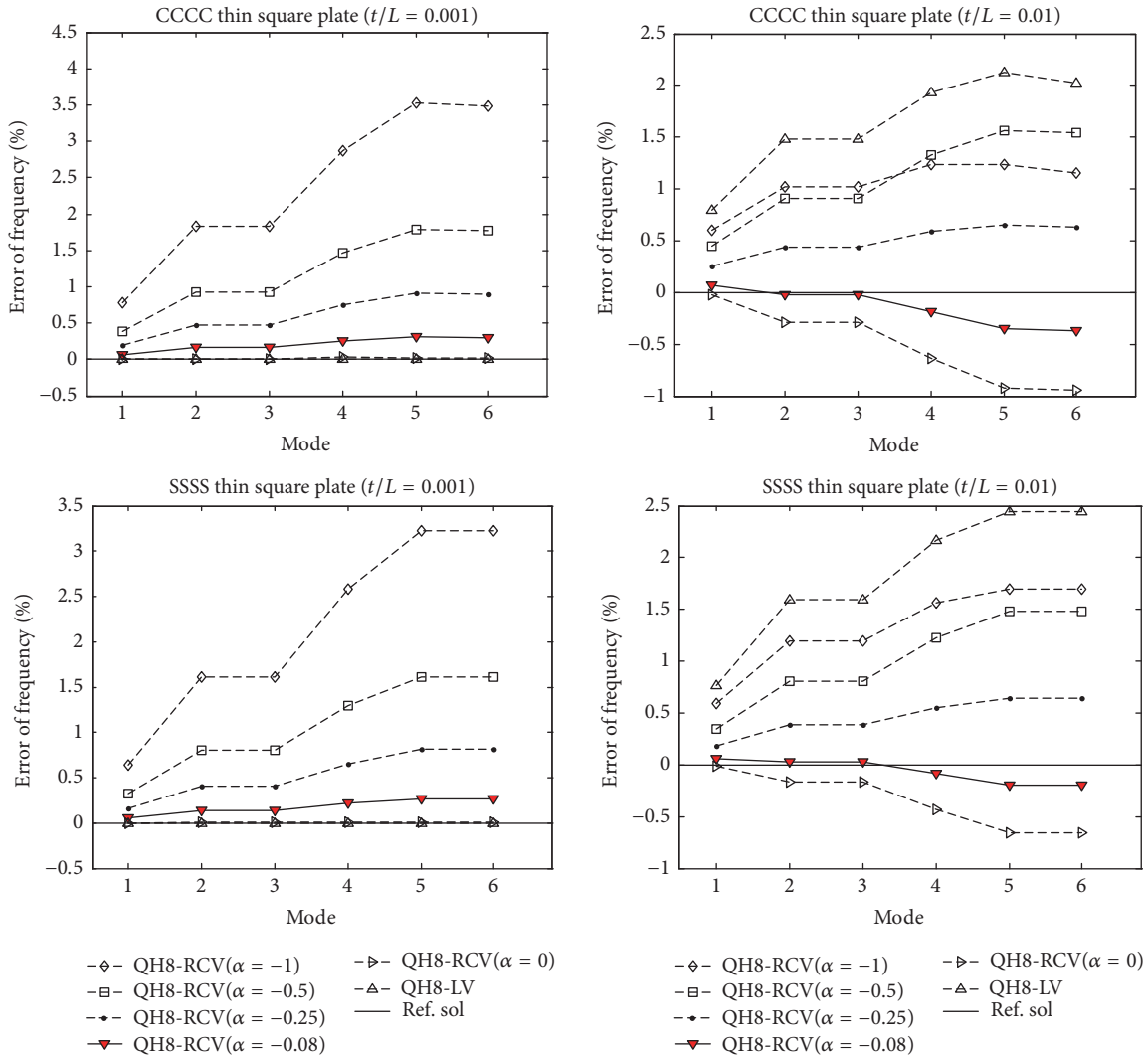

Figure 4: Error of six lowest nondimensional frequency parameters.

4.2.2. Free Vibration of Circular Plate. Free vibration of a circular plate (Figure 7) of $R = 5$ with the clamped boundary is then studied in this subsection. The material parameters of the circular plate are given as follows: the density mass $\rho = 8000$, Young's modulus $E = 2.0 \times 10^{11}$, and Poisson's ratio $\mu = 0.3$.

60 proposed elements and 205 nodes as shown in Figure 7, Mesh A, are used to discretize the whole plate for S8R of Abaqus, QH8-RCV(−0.08) and QH8-LV, while the compared solutions given by other elements employ even finer meshes. The frequencies given by MIN3 and NS+ES-FEM [51] employ a mesh of 394 elements and 222 nodes; the solutions of NS-DSG and ES-FEM+DSG3 employ a much finer mesh of 848 elements and 460 nodes and ANS4 [52] using 432 quadrilateral plate elements (or 864 triangular elements).

The first ten modes of thin ($t/2R = 0.01$) and thick ($t/2R = 0.1$) circular plates are shown in Tables 10 and 11, respectively. Figure 8 plots the results obtained from different methods. It is observed that the QH8-RCV and QH8-LV are good competitors to ANS4 and exact solutions [42, 43] and is more accurate than MIN3, ES-FEM+DSG3, and NS+ES-FEM.

First six lowest modes of this clamped circular obtained from QH8-RCV using the mesh of Figure 7 Mesh B are shown in Figure 9, which exactly describes the real physical modes of the circular plate.

4.2.3. Free Vibration of Triangular Plates. QH8-RCV ($\alpha = -0.08$) and QH8-LV are then applied in the free vibration analyses of a cantilever triangular plate (CFF) with various shape geometries just as shown in Figure 10(a). The material parameters of the triangular plate are given as follows: the density mass $\rho = 8000$, Young's modulus $E = 2.0 \times 10^{11}$, and Poisson's ratio $\mu = 0.3$. The plate is discretized by the meshes as shown in Figure 10 for QH8. The convergence study of

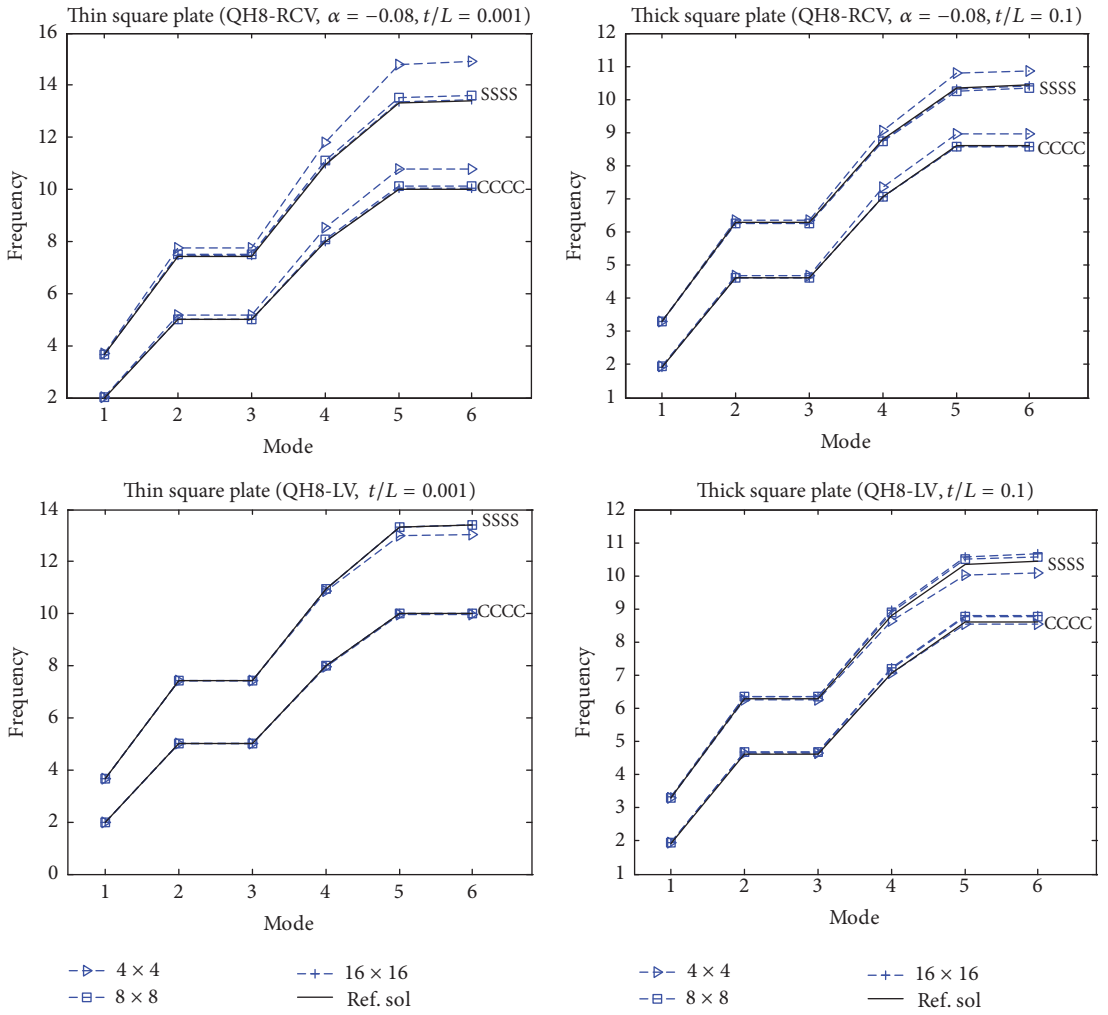

FIGURE 5: Convergence of six lowest nondimensional frequency parameters (t/h = 0.001, 0.1, and SSSS, CCCC).

nondimensional frequency parameter $\overline{\omega} = \omega L^2\sqrt{\rho t/D}/\pi^2$ for thin ($t/L = 0.001$) and thick ($t/L = 0.2$) triangular plates against different skew angles $\alpha = 0^\circ, 15^\circ, 30^\circ, 45^\circ$, and 60° is undertaken and shown in Tables 12 and 13, respectively. The first four nondimensional frequency parameters for the thin and thick triangular plates are plotted in Figures 11 and 12.

The NS+ES-FEM [51] with the mesh of 170 triangular elements and 108 nodes and DSG3, MIN3, and ES-FEM+DSG3 are also used for comparison. The reference solution was obtained by the ANS method [52] using a mesh of 796 triangular elements. For thick triangular plate, QH8-RCV's performance is the best, but QH8-LV provides worse result when the angle becomes larger for the third and fourth modes in Figure 12, because of the mesh with small number of elements (45°, 26 elements and 60°, 28 elements) in some degree. For the thin triangular plate, QH8-LV is better than DSG3 and MIN3 and competes well with NS+ES-FEM and Rayleigh-Ritz [53]. QH8-RCV's performance is still the best and a strong competitor of Rayleigh-Ritz. Six lowest modes of cantilever triangular plates (CFF) obtained from QH8-RCV are illustrated in Figure 13.

4.3. Critical Load of Buckling. In the following tests, we perform a series of plate buckling analyses to assess the convergence characteristics and accuracy of the developed QH8 element in predicting a critical buckling load. The results are presented in terms of a nondimensional buckling load intensity factor.

$$K_b = \frac{\lambda b^2}{(\pi^2 D)}, \tag{47}$$

with b being the edge width of the plate that is used throughout the paper and $D = Et^3/12(1-\mu^2)$.

4.3.1. Rectangular Plates Subjected to an In-Plane Compressive Load. The parameter α_0 in (42) for the present element

Table 9: Frequency parameters for square Mindlin plates with different boundary conditions.

Boundary	t/b	Element	Mode sequence number					
			1	2	3	4	5	6
SSFF	0.001	QH8-RCV	0.3407	1.7530	1.9541	3.8675	5.1729	5.4231
		QH8-LV	0.3405	1.7485	1.9504	3.8550	5.1471	5.4000
		Ref. sol	0.341	1.754	1.955	3.872	5.171	5.419
	0.1	QH8-RCV	0.3329	1.6780	1.8751	3.5579	4.7179	4.9445
		QH8-LV	0.3335	1.6944	1.8922	3.6122	4.8227	5.0496
		Ref. sol	0.333	1.677	1.874	3.557	4.718	4.945
SFSF	0.001	QH8-RCV	0.9759	1.6329	3.7170	3.9486	4.7357	7.1656
		QH8-LV	0.9755	1.6303	3.7009	3.9431	4.7240	7.1313
		Ref. sol	0.976	1.635	3.721	3.946	4.735	7.167
	0.1	QH8-RCV	0.9567	1.5594	3.4297	3.6829	4.3331	6.2859
		QH8-LV	0.9601	1.5703	3.4900	3.7305	4.4011	6.4372
		Ref. sol	0.956	1.559	3.429	3.681	4.332	6.290
SCSC	0.001	QH8-RCV	2.9350	5.5542	7.0348	9.6060	10.3849	13.1192
		QH8-LV	2.9333	5.5466	7.0242	9.5833	10.3566	13.0799
		Ref. sol	2.933	5.547	7.024	9.583	10.356	13.080
	0.1	QH8-RCV	2.7019	4.9725	5.9898	7.9621	8.7685	10.2141
		QH8-LV	2.7212	5.0501	6.0804	8.1367	8.9997	10.4651
		Ref. sol	2.700	4.971	5.990	7.972	8.787	10.249
CFFF	0.001	QH8-RCV	0.3516	0.8603	2.1563	2.7540	3.1315	5.4804
		QH8-LV	0.3514	0.8590	2.1499	2.7427	3.1211	5.4505
		Ref. sol	0.352	0.862	2.157	2.756	3.136	5.490
	0.1	QH8-RCV	0.3476	0.8167	2.0353	2.5832	2.8610	4.8108
		QH8-LV	0.3481	0.8205	2.0567	2.6220	2.8963	4.9106
		Ref. sol	0.348	0.816	2.034	2.582	2.860	4.811
CCFF	0.001	QH8-RCV	0.7003	2.4197	2.6929	4.8226	6.3563	6.6444
		QH8-LV	0.6997	2.4117	2.6870	4.8039	6.3216	6.6129
		Ref. sol	0.701	2.422	2.694	4.828	6.353	6.640
	0.1	QH8-RCV	0.6761	2.2434	2.5046	4.2523	5.5551	5.8093
		QH8-LV	0.6777	2.2687	2.5294	4.3213	5.6786	5.9314
		Ref. sol	0.676	2.242	2.503	4.251	5.557	5.812
CFCF	0.001	QH8-RCV	2.2459	2.6732	4.4127	6.2028	6.8074	8.0892
		QH8-LV	2.2448	2.6689	4.3935	6.1928	6.7890	8.0240
		Ref. sol	2.246	2.675	4.417	6.198	6.806	8.087
	0.1	QH8-RCV	2.0899	2.4334	3.9032	5.3315	5.7707	6.9214
		QH8-LV	2.0979	2.4508	3.9716	5.3982	5.8585	7.1420
		Ref. sol	2.088	2.431	3.901	5.331	5.771	6.929

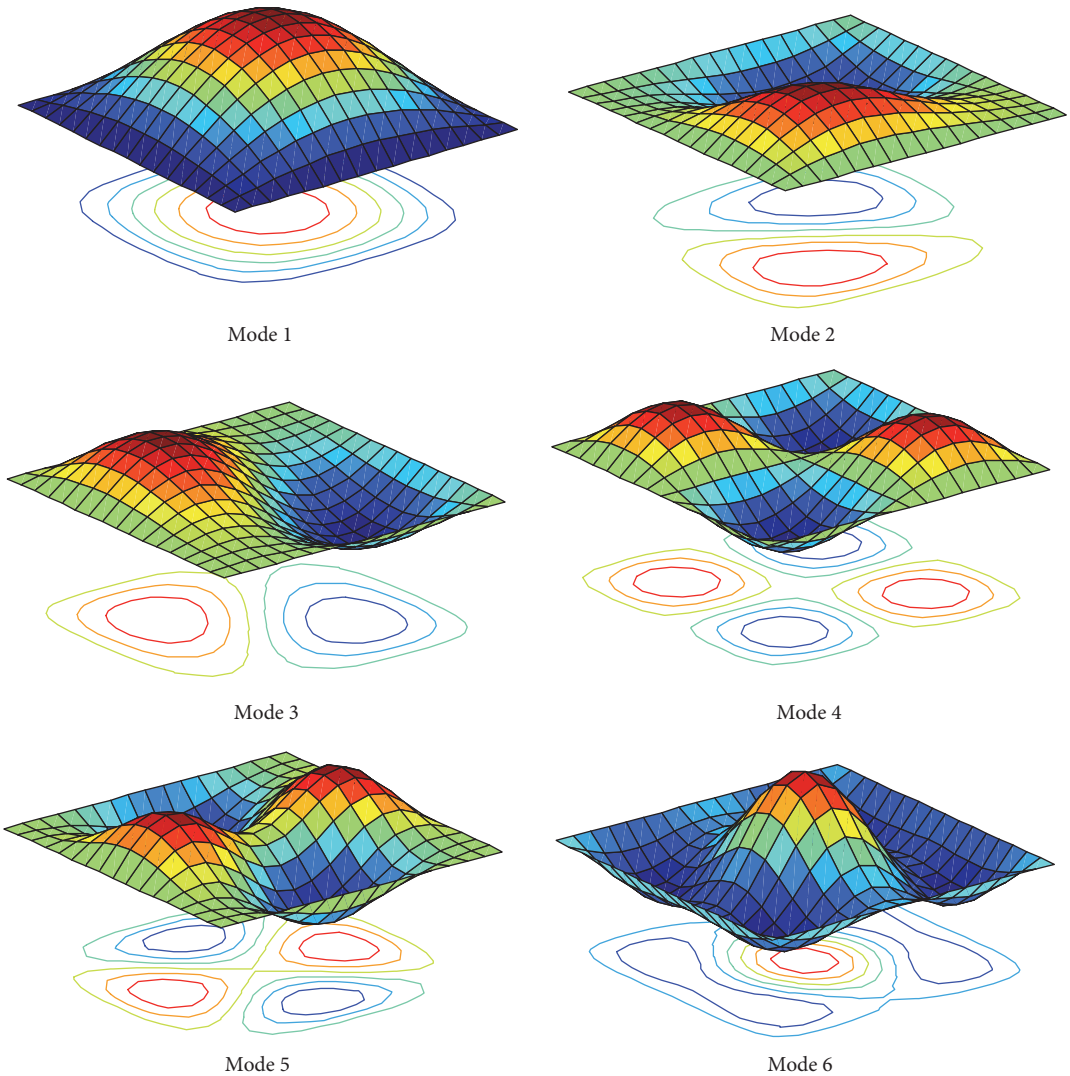

Figure 6: Shape of the six lowest modes of SSSS thin square plate obtained from QH8-RCV ($\alpha = -0.08$, $t/h = 0.001$).

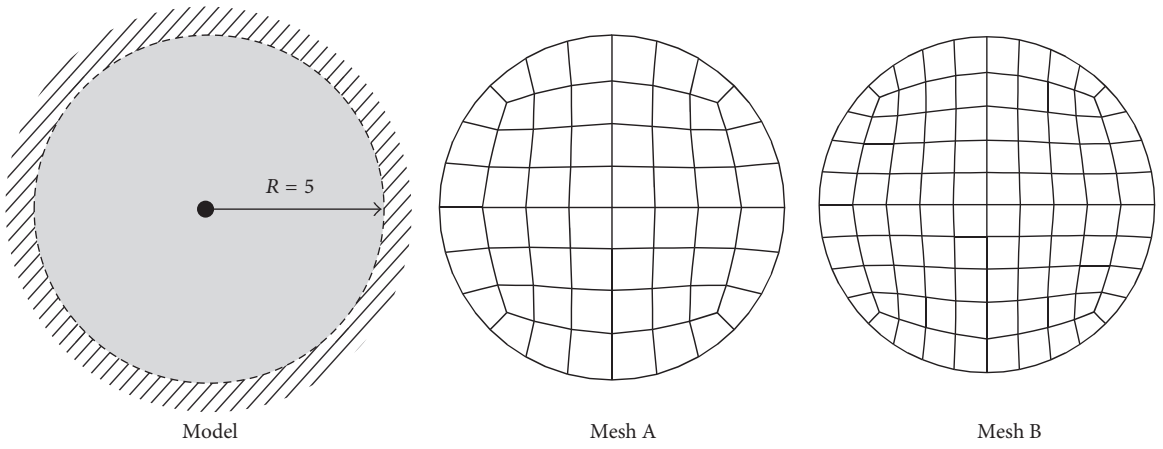

Figure 7: Circular plate model and its discretization for QH8 element (Mesh A: 205 nodes, 60 elements; Mesh B: 321 nodes, 96 elements).

Table 10: Ten lowest parameterized natural frequencies $\overline{\omega} = \omega R^2 \sqrt{\rho t/D}$ of a clamped circular plate with $t/2R = 0.01$.

Mode	NS-ES-FEM	S8R	MIN3	ES-FEM+DSG3	ANS4	QH8-RCV	QH8-LV	Ref. sol [42]
1	10.2700	10.3095	10.4082	10.3109	10.2572	10.3613	10.3669	10.216
2	21.1535	21.4233	22.2198	21.6702	21.4981	21.6355	21.5152	21.260
3	21.1617	21.4283	22.2444	21.6900	21.4981	21.6356	21.5167	21.260
4	34.4423	35.2809	37.7461	36.3124	35.3941	35.6621	35.1192	34.880
5	34.4573	35.3685	37.7816	36.3816	35.5173	35.7071	35.2812	34.880
6	39.1472	40.1039	43.0344	41.3801	40.8975	40.7676	40.1565	39.771
7	49.6819	52.2399	57.8881	54.7796	52.2054	52.6337	51.3212	51.040
8	49.7157	52.2597	58.0836	54.8922	52.2054	52.6344	51.3358	51.040
9	58.8517	62.2179	68.7260	64.6300	63.2397	63.0358	61.0974	60.820
10	59.0184	62.2543	69.2354	65.1330	63.2397	63.0368	61.1017	60.820

Table 11: Ten lowest parameterized natural frequencies $\overline{\omega} = \omega R^2 \sqrt{\rho t/D}$ of a clamped circular plate with $t/2R = 0.1$.

Mode	NS-ES-FEM	S8R	MIN3	ES-FEM+DSG3	ANS4	QH8-RCV	QH8-LV	Ref. sol [43]
1	9.2460	9.2539	9.9682	9.3262	9.2605	9.3380	9.4444	9.240
2	17.6424	17.8115	20.306	18.0461	17.9469	17.8602	18.1926	17.834
3	17.6461	17.8115	20.3256	18.0673	17.9469	17.8603	18.1938	17.834
4	26.5699	27.0923	32.7800	27.8438	27.0345	26.9746	27.5602	27.214
5	26.5740	27.1650	32.7905	27.8856	27.6566	26.9836	27.6854	27.214
6	29.7654	30.4101	37.1591	31.1280	30.3221	30.0846	30.8631	30.211
7	35.5595	33.8815	47.5437	38.6936	37.2579	36.5419	37.3990	37.109
8	35.5999	33.8848	47.5993	38.7042	37.2579	36.5431	37.4096	37.109
9	41.0560	37.0290	55.3530	44.1130	43.2702	41.8999	42.8445	42.409
10	41.1226	37.0324	55.6608	44.3286	43.2702	41.9011	42.8465	42.409

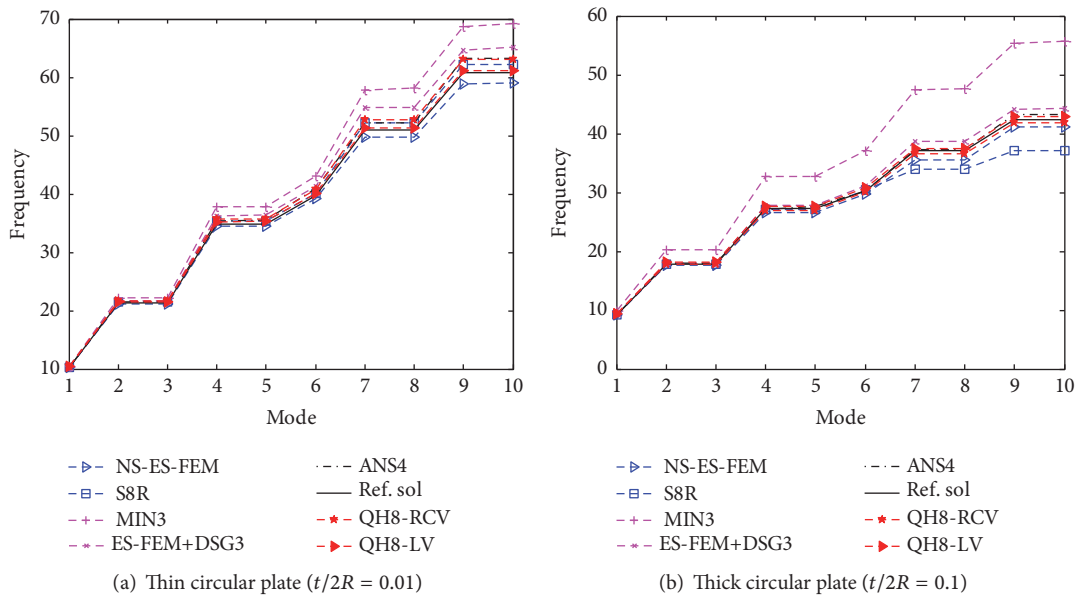

(a) Thin circular plate ($t/2R = 0.01$) (b) Thick circular plate ($t/2R = 0.1$)

Figure 8: Ten lowest parameterized natural frequencies of a clamped circular plate.

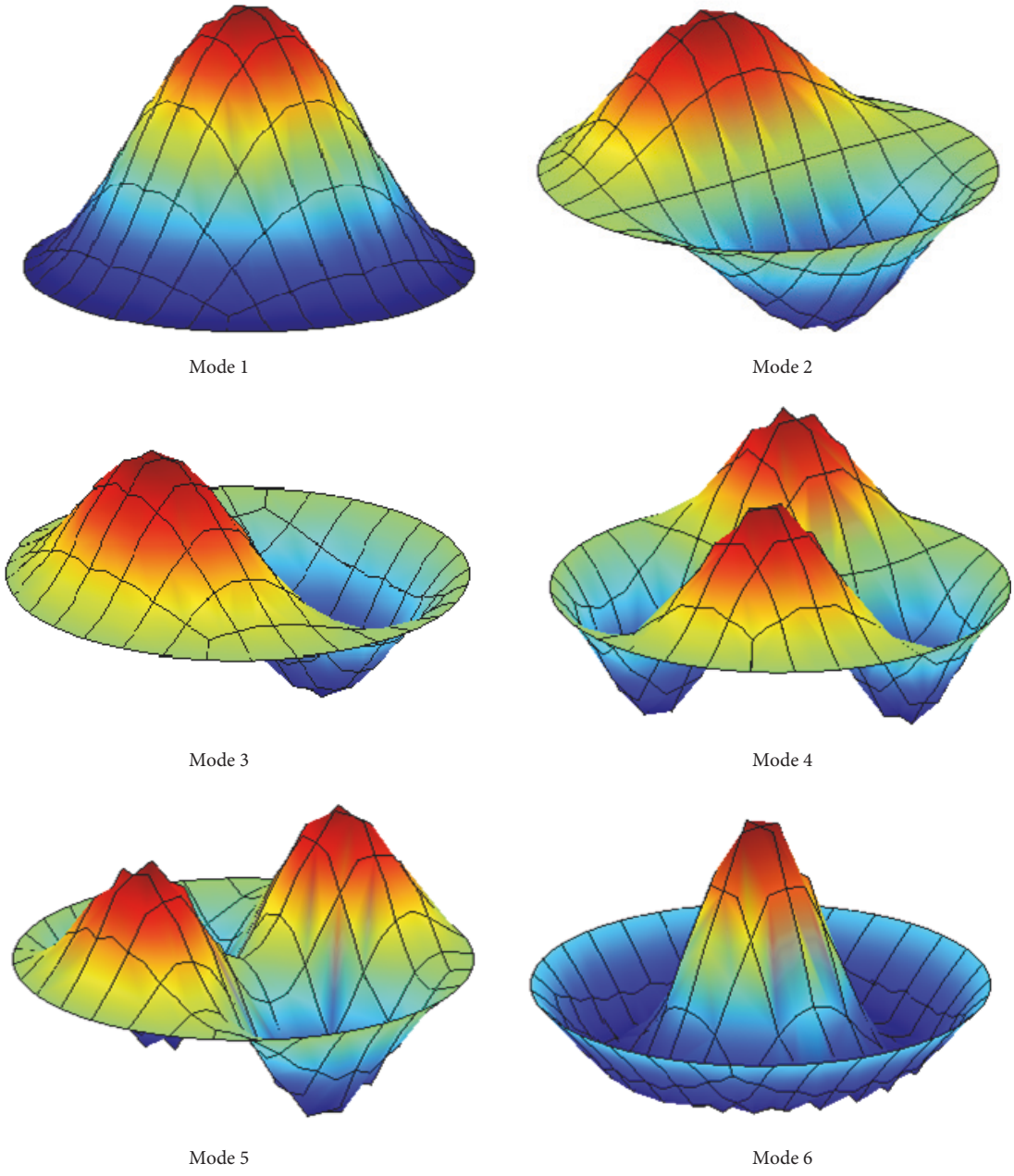

Figure 9: Shape of the six lowest modes of a clamped thick circular plate obtained from QH8-RCV ($t/2R = 0.1$).

QH8-R (8-node hybrid element with refined geometric stiffness matrix) is determined by comparison using numerical examples. A square plate ($a/b = 1$) compressed in one direction or two perpendicular directions are divided into different meshes 2×2, 4×4, 6×6, 8×8, 12×12, 16×16. Thickness-to-width aspect ratios $t/b = 0.01, 0.1$, $\alpha_0 = -1, -0.75, -0.5, -0.3, -0.17, 0$, and boundary conditions SSSS, CCCC are chosen. The computational results of the critical load are given in Tables 14 and 15 and Figure 14, in which the exact solutions can be found in [44–46]. After analysis of numerical examples, the present 8-node hybrid stress element QH8-R(α_0) has higher accuracy when $-0.4 \leq \alpha_0 \leq -0.1$, and we advise $\alpha_0 = -0.17$ for following numerical examples.

A shear-locking phenomenon is firmly involved when using thick plate theories to analyze thin plates. The present QH8 element is free of shear-locking in static calculation. A square plate is considered for this purpose and all other related parameters are taken exactly the same as above. Various boundaries such as SSSS, SFSC, SFSS, and SFSF

Table 12: The lowest six parameterized natural frequencies of triangular plates with $t/L = 0.001$.

Skew angle	Method	Mode sequence number					
		1	2	3	4	5	6
0°	DSG3	0.6288	2.4399	3.4796	5.9913	8.3737	11.2081
	MIN3	0.6272	2.4242	3.4344	5.9458	8.2460	11.0178
	ES-FEM+DSG3	0.6241	2.3970	3.3631	5.7976	7.9696	10.5356
	NS+ES-FEM	0.6253	2.3335	3.1888	5.4772	7.4350	9.2790
	Rayleigh-Ritz	0.6240	2.3770	3.3080	5.6890	7.7430	—
	ASN4	0.6240	2.3790	3.3170	5.7240	7.7940	10.2000
	QH8-RCV	0.6232	2.3709	3.2980	5.6766	7.7627	10.0574
	QH8-LV	0.6165	2.3143	3.1843	5.4810	7.5749	9.6271
15°	DSG3	0.5915	2.2360	3.6467	5.5686	7.8875	11.1572
	MIN3	0.5886	2.2229	3.5717	5.5286	7.7447	10.9544
	ES-FEM+DSG3	0.5843	2.1979	3.4937	5.3893	7.4745	10.4532
	NS+ES-FEM	0.5854	2.1449	3.2938	5.0391	7.0313	9.1652
	Rayleigh-Ritz	0.5840	2.1810	3.4090	5.2800	7.2640	—
	ASN4	0.5830	2.1810	3.4130	5.3030	7.2890	10.0950
	QH8-RCV	0.5829	2.1759	3.3995	5.2687	7.2983	9.9691
	QH8-LV	0.5750	2.1291	3.2332	5.0577	7.0972	9.4300
30°	DSG3	0.5928	2.2293	3.9729	5.8523	7.8772	11.9930
	MIN3	0.5866	2.2164	3.8656	5.8059	7.6697	11.5791
	ES-FEM+DSG3	0.5795	2.1881	3.7620	5.6464	7.3608	10.9609
	NS+ES-FEM	0.5801	2.1433	3.5402	5.2019	6.8932	9.6373
	Rayleigh-Ritz	0.5760	2.1740	3.6390	5.5110	7.1080	—
	ASN4	0.5750	2.1740	3.6380	5.5340	7.1390	10.4770
	QH8-RCV	0.5763	2.1685	3.6379	5.4957	7.1296	10.3946
	QH8-LV	0.5714	2.1368	3.5544	5.3345	6.9689	9.9234
45°	DSG3	0.6265	2.4298	4.5709	6.9888	8.7055	13.4984
	MIN3	0.6125	2.4038	4.4237	6.9194	8.3447	12.7848
	ES-FEM+DSG3	0.6001	2.3557	4.2652	6.6442	7.9210	11.8923
	NS+ES-FEM	0.6020	2.3189	4.0352	6.0299	7.3322	10.5988
	Rayleigh-Ritz	0.5900	2.3290	4.1370	6.3810	7.6020	—
	ASN4	0.5880	2.3240	4.1260	6.3810	7.6140	11.2240
	QH8-RCV	0.5925	2.3290	4.1374	6.4133	7.6019	11.2205
	QH8-LV	0.5858	2.3042	3.9784	6.1554	7.4240	10.8429
60°	DSG3	0.6969	2.9282	6.0785	9.3379	11.8340	17.8590
	MIN3	0.6631	2.8106	5.8343	8.9727	11.3197	16.3597
	ES-FEM+DSG3	0.6371	2.6804	5.4909	8.1353	10.6516	14.5225
	NS+ES-FEM	0.6546	2.6792	5.3330	7.3384	9.6825	12.9900
	Rayleigh-Ritz	0.6170	2.5760	5.3760	7.5240	10.2850	—
	ASN4	0.6130	2.5640	5.3530	7.4600	10.3060	12.9420
	QH8-RCV	0.6234	2.5978	5.3502	7.5829	10.2623	13.0926
	QH8-LV	0.6164	2.5712	5.1891	7.3141	9.8462	12.8085

Table 13: The lowest six parameterized natural frequencies of triangular plates with $t/L = 0.2$.

Skew angle	Method	Mode sequence number					
		1	2	3	4	5	6
0°	DSG3	0.5872	1.9529	2.4678	4.1305	5.2243	6.2886
	MIN3	0.6042	2.1109	2.7737	4.6581	6.1311	7.3208
	ES-FEM+DSG3	0.5856	1.9376	2.4411	4.0678	5.1289	6.1359
	Rayleigh-Ritz	0.5820	1.9000	2.4080	3.9360	—	—
	ASN4	0.5820	1.9150	2.4280	3.9840	5.0180	5.9440
	NS+ES-FEM	0.5821	1.8710	2.3600	3.8330	4.8217	5.5683
	QH8-RCV	0.5821	1.8907	2.3931	3.8677	4.8701	5.6897
	QH8-LV	0.5826	1.9628	2.5320	4.1115	5.2710	6.4029
15°	DSG3	0.5478	1.8160	2.4429	3.8111	5.0253	6.0033
	MIN3	0.5656	1.9555	2.7772	4.2851	5.8857	6.9977
	ES-FEM+DSG3	0.5457	1.8018	2.4121	3.7529	4.9317	5.8327
	Rayleigh-Ritz	0.5440	1.7710	2.3860	3.6280	—	—
	ASN4	0.5450	1.7640	2.4200	3.6080	4.8200	5.4310
	NS+ES-FEM	0.5442	1.7466	2.3391	3.5289	4.6721	5.1901
	QH8-RCV	0.5441	1.7644	2.3687	3.5813	4.7024	5.3504
	QH8-LV	0.5427	1.8251	2.5244	3.8353	5.0144	6.1823
30°	DSG3	0.5365	1.8126	2.4954	3.7549	4.9796	5.9219
	MIN3	0.5582	1.9551	2.8595	4.2605	5.8273	6.9945
	ES-FEM+DSG3	0.5329	1.7963	2.4552	3.6902	4.8717	5.6942
	Rayleigh-Ritz	0.5330	1.7720	2.4190	3.5650	—	—
	ASN4	0.5320	1.7730	2.4370	3.5910	4.7650	5.3230
	NS+ES-FEM	0.5336	1.7485	2.3730	3.4615	4.5927	4.9630
	QH8-RCV	0.5331	1.7663	2.4045	3.5167	4.6384	5.1512
	QH8-LV	0.5342	1.8391	2.7165	3.9146	4.9778	6.4454
45°	DSG3	0.5448	1.9269	2.6246	3.9196	5.1474	5.9838
	MIN3	0.5724	2.1044	3.0165	4.5535	6.0525	7.2736
	ES-FEM+DSG3	0.5380	1.9002	2.5682	3.8239	4.9806	5.6000
	Rayleigh-Ritz	0.5400	1.8850	2.4890	3.6740	—	—
	ASN4	0.5410	1.8840	2.5180	3.7480	4.7400	5.2920
	NS+ES-FEM	0.5408	1.8634	2.4323	3.5593	4.4299	4.9328
	QH8-RCV	0.5391	1.8765	2.4729	3.6337	4.5699	5.0583
	QH8-LV	0.5389	1.9562	2.9904	4.2186	5.2159	6.9240
60°	DSG3	0.5691	2.1281	2.7093	4.3427	5.3437	6.5278
	MIN3	0.6017	2.3742	3.2377	5.1762	6.5578	8.1003
	ES-FEM+DSG3	0.5569	2.0692	2.5955	4.1109	4.7967	6.0192
	Rayleigh-Ritz	0.5590	2.0590	2.3960	3.5900	—	—
	ASN4	0.5590	2.0950	2.4830	3.9100	4.5170	5.7630
	NS+ES-FEM	0.5611	2.0446	2.3276	3.5969	4.2312	5.3615
	QH8-RCV	0.5574	2.0455	2.3807	3.6046	4.2131	5.2640
	QH8-LV	0.5573	2.1170	3.8244	4.6656	6.2099	7.7794

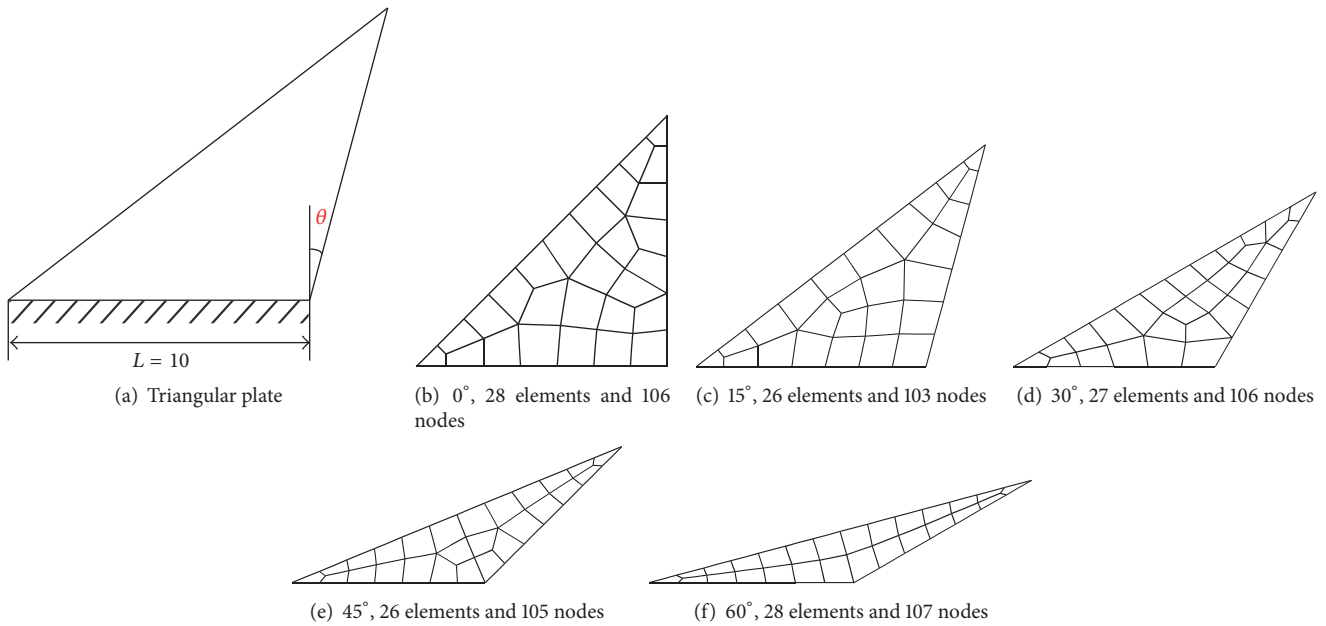

(a) Triangular plate (b) 0°, 28 elements and 106 nodes (c) 15°, 26 elements and 103 nodes (d) 30°, 27 elements and 106 nodes

(e) 45°, 26 elements and 105 nodes (f) 60°, 28 elements and 107 nodes

Figure 10: Triangular plate model with various shape geometries and its discretization meshes ($\theta = 0^\circ, 15^\circ, 30^\circ, 45^\circ, 60^\circ$).

Table 14: The factor of uniaxial buckling loads along the x-axis of rectangular plates with length-to-width aspect ratios $a/b = 1$ and thickness-to-width aspect ratios $t/b = 0.01$.

Boundary condition	Element (α_0)	Mesh					
		2 × 2	4 × 4	6 × 6	8 × 8	12 × 12	16 × 16
SSSS	QH8-R(−1)	3.1427	3.4982	3.7191	3.8183	3.8982	3.9293
	(−0.75)	4.0364	3.8502	3.9045	3.9338	3.9588	3.9691
	(−0.5)	4.7314	4.0776	4.0190	4.0043	3.9961	3.9940
	(−0.3)	4.8659	4.1389	4.0521	4.0258	4.0084	4.0027
	(−0.17)	4.7097	4.1161	4.0444	4.0225	4.0079	4.0031
	(0)	4.2694	4.0139	4.0002	3.9980	3.9972	3.9971
	Reference [44]	4					
CCCC	QH8-R(−1)	5.3071	7.4051	8.3520	8.9070	9.4027	9.6049
	(−0.75)	8.2670	9.1692	9.4445	9.6292	9.7956	9.8651
	(−0.5)	10.9935	10.6774	10.2199	10.1074	10.0459	10.0304
	(−0.3)	12.9592	11.1920	10.4649	10.2587	10.1293	10.0885
	(−0.17)	13.6765	11.0371	10.4113	10.2349	10.1247	10.0896
	(0)	13.6316	10.2573	10.0875	10.0576	10.0482	10.0472
	Reference [44]	10.0738					

Note. $\kappa = 5/6$.

are investigated. Several thickness-span aspect ratios $t/b = 0.1, 0.2$ (moderately thick plate) and $t/b = 0.001, 0.05$ (thin plate) are considered, respectively, and the results are shown in Table 16 and Figure 15, which are compared with the analytical solutions [45] and other existing numerical approaches such as the SSM [54] and the shear-locking-free and mesh-free method (Shear-MK, MK) [55]. The element S8R and QH8-R use a regular pattern of 11 × 11 element (408

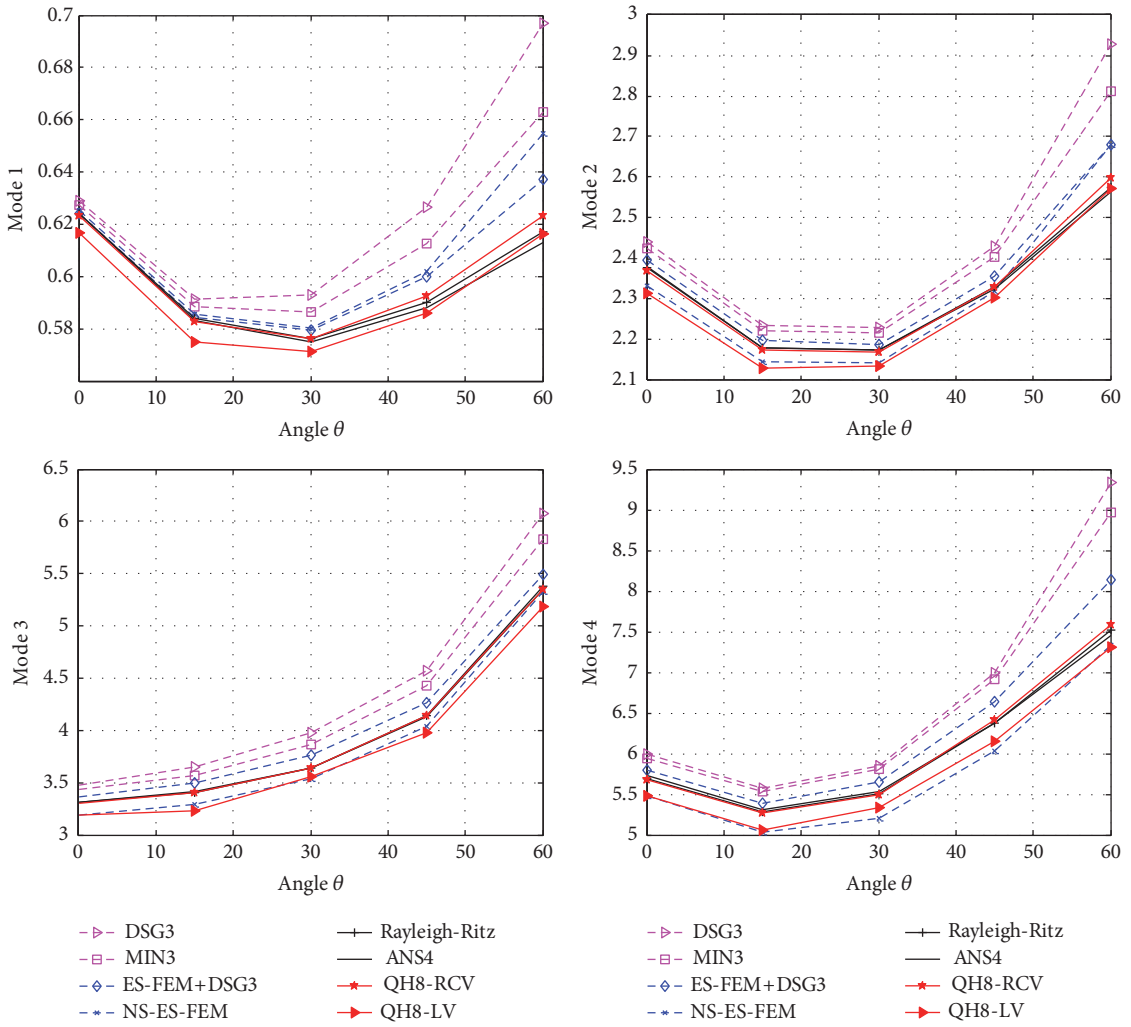

FIGURE 11: Convergence study of the lowest four parameterized natural frequencies of triangular plates with $t/L = 0.001$.

TABLE 15: The factor of uniaxial buckling loads along the x-axis of rectangular plates with length-to-width aspect ratios $a/b = 1$ and thickness-to-width aspect ratios $t/b = 0.1$.

Boundary	Element (α_0)	Mesh					
		2 × 2	4 × 4	6 × 6	8 × 8	12 × 12	16 × 16
SSSS	QH8-R(−1)	2.3811	2.4760	2.7861	3.0392	3.3424	3.4914
	(−0.75)	3.3240	3.0601	3.2413	3.3983	3.5815	3.6689
	(−0.5)	4.1951	3.5827	3.6110	3.6676	3.7403	3.7756
	(−0.3)	4.4995	3.8245	3.7755	3.7778	3.7917	3.8002
	(−0.17)	4.3933	3.8501	3.7970	3.7869	3.7845	3.7850
	(0)	3.9119	3.6966	3.7056	3.7146	3.7232	3.7266
	Reference [45]	3.7864					
CCCC	QH8-R(−1)	3.4293	4.0301	4.6232	5.2042	6.1652	6.7926
	(−0.75)	5.9999	5.8082	6.0193	6.4602	7.1856	7.6362
	(−0.5)	8.7108	7.7026	7.4918	7.6519	7.9938	8.2101
	(−0.3)	10.4843	8.8128	8.3089	8.2536	8.3146	8.3741
	(−0.17)	10.9492	8.8625	8.3903	8.2963	8.2811	8.2936
	(0)	9.9368	7.5669	7.5101	7.5613	7.6923	7.7874
	Reference [46]	8.2917					

Note. $\kappa = 5/6$.

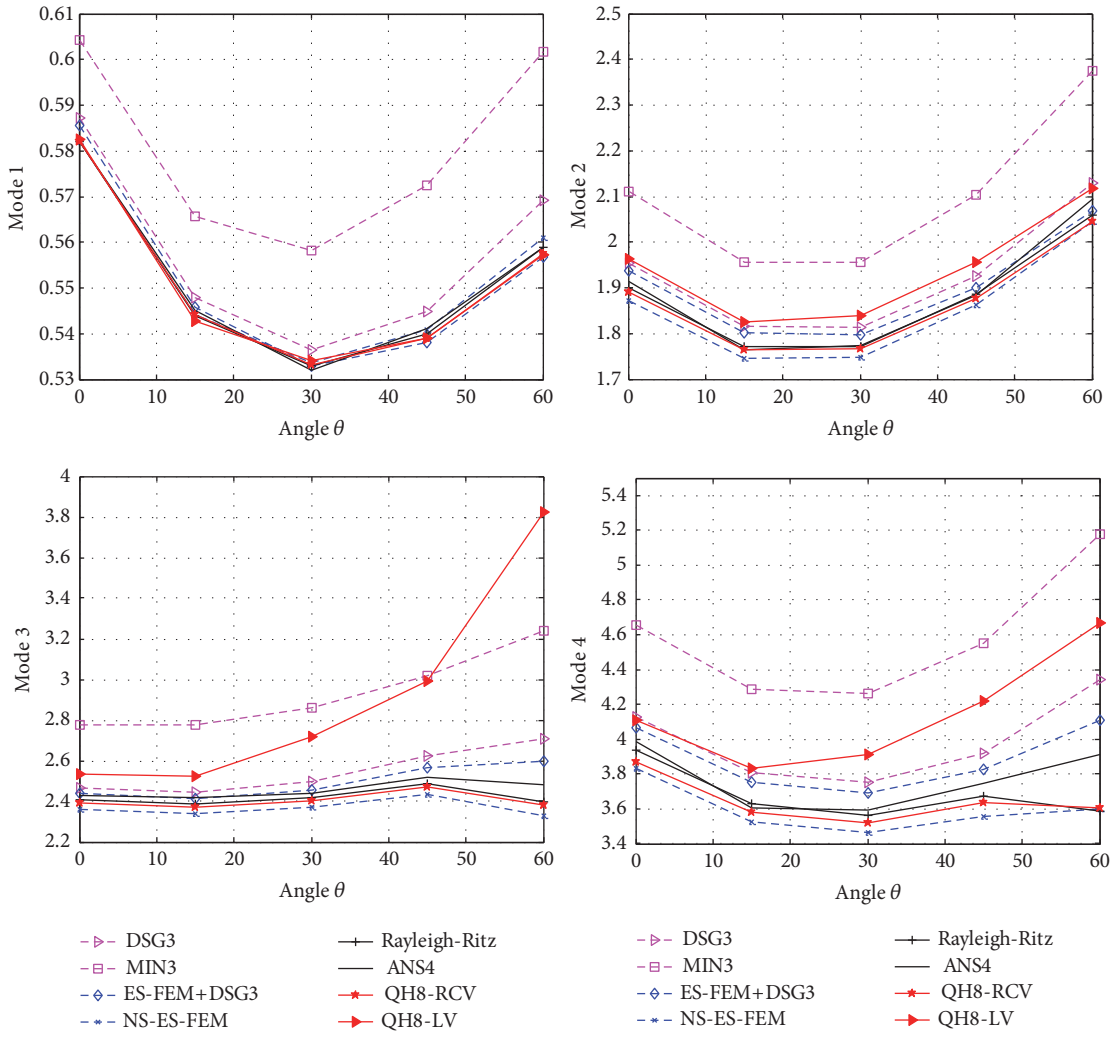

Figure 12: Convergence study of the lowest four parameterized natural frequencies of triangular plates with $t/L = 0.2$.

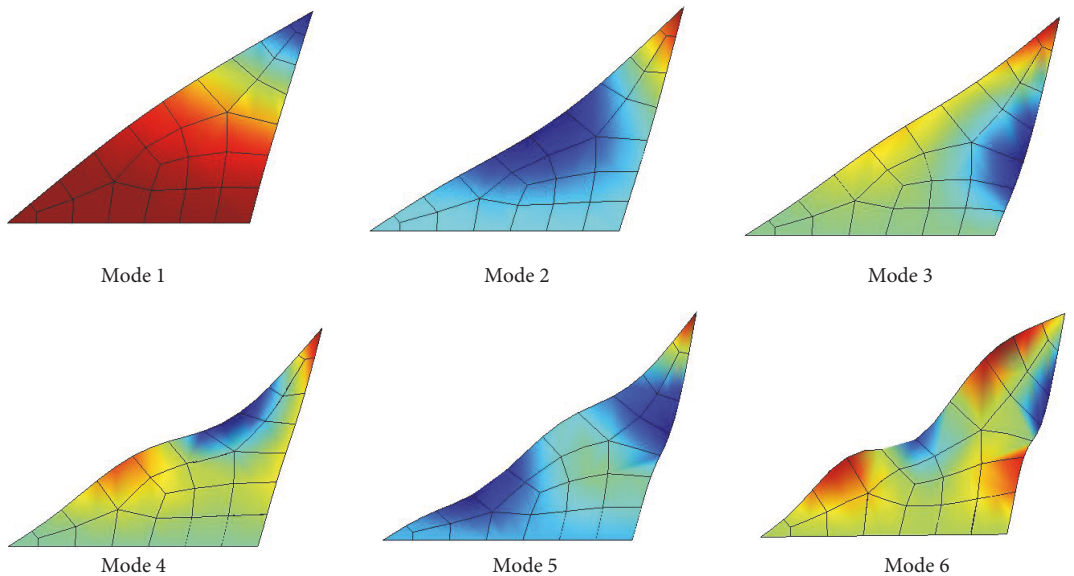

Figure 13: The six lowest modes of a CFF thin triangular plate obtained from QH8-RCV ($\theta = 15^\circ$).

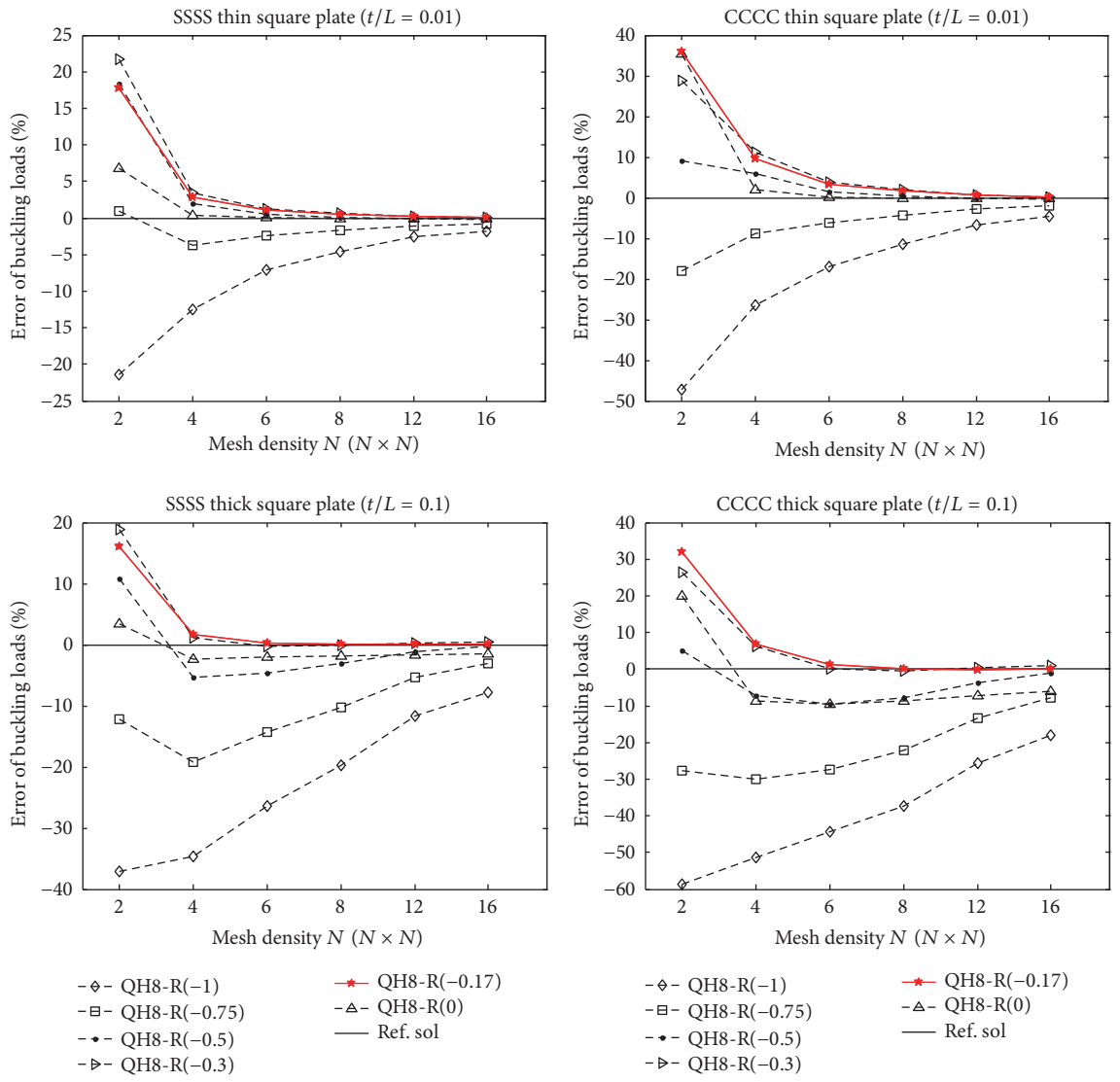

FIGURE 14: The factor of uniaxial buckling loads ($\sigma_x{}^0$) along the x-axis of rectangular plates for QH8-R (α_0) element.

nodes) and MK, Shear-MK use a regular pattern of 21 × 21 elements (441 nodes). A shear correction factor $\kappa = \pi^2/12$ is used here for a proper comparison.

Through the achieved results shown in Table 16 and Figure 15, the shear-locking phenomenon, on the one side, is found very clearly because of losing the accuracy significantly when the standard MK is applied to deal with thin plates, that is, t/b = 0.001, 0.05, but conversely matches well with thick plates, that is, t/b = 0.1, 0.2. Higher buckling loads by the standard MK are obtained because the plates may exhibit highly stiffer behavior. On the other hand, a good agreement and free of shear-locking are found when the Shear-MK, S8R, and the present QH8-R are used.

The results of uniaxial buckling loads ($\sigma_y{}^0$) along the y-axis and the biaxial in-plane compression load ($\sigma_x{}^0 = \sigma_y{}^0$) are shown in Tables 17 and 18 and Figures 16 and 17 associated with five different densities of regular elements such as 2 × 2 (21 nodes), 4×4 (65 nodes), 6×6 (133 nodes), 8×8 (225 nodes), and 10 × 10 (341 nodes).

We also consider simply supported plates (SSSS) with various thickness-to-width ratios, t/b = 0.05, 0.1, 0.2, and length-to-width ratios, a/b = 0.5, 1.0, 1.5, 2.0, 2.5.

Table 19 and Figure 18 show the buckling factors using the element QH8-R with regular mesh of 9 × 9 rectangular elements (280 nodes) when a/b = 1.0. The QH8-R results are also compared to the DSG3 and ES-DSG3 [47] (mesh of 16 × 16 elements and 289 nodes), S8R (mesh of 9 × 9 elements and 280 nodes), mesh-free method [48], and the pb-2 Ritz [46]. It is seen that the QH8-R exhibits a good agreement with the pb-2 Ritz method, and S8R is not suitable for plate t/b = 0.2. Figure 19 also depicts the uniaxial buckling modes of simply supported rectangular plates with thickness-to- width

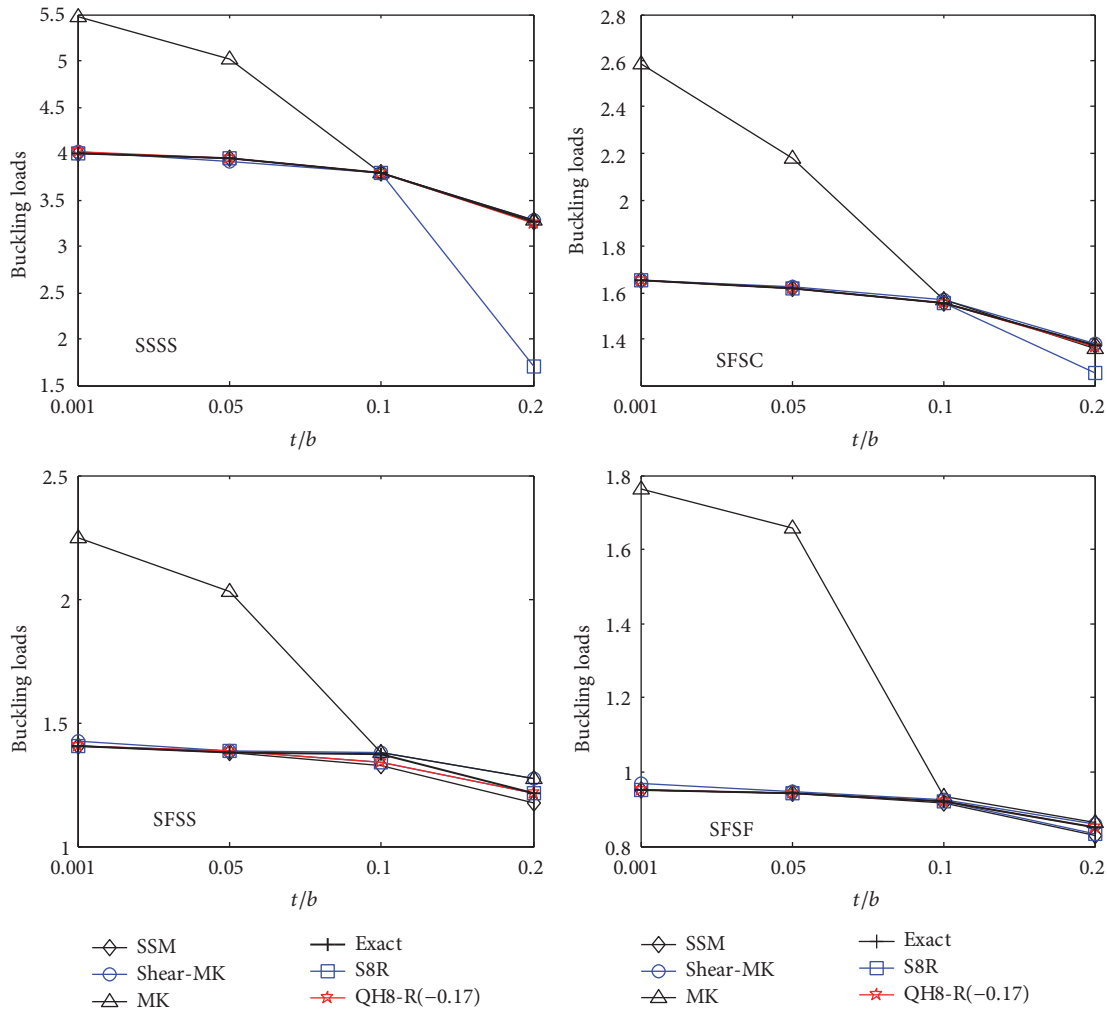

FIGURE 15: Normalized uniaxial buckling load factors along the x-axis ($\sigma_x{}^0$) versus the thickness-span aspect ratio t/b = 0.001, 0.05, 0.1, 0.2 with various boundaries.

ratios $t/b = 0.01$ and various length-to-width ratios, $a/b = 1.0$, 1.5, 2.0, 2.5.

4.3.2. Compression Buckling Behavior of Skew Plates. The buckling problem of skew plate has also been considered by Kitipornchai et al. [46] and Wang et al. [56] using the pb-2 Ritz method. Skew plates, as shown in Figure 20, with skew angle, θ, thickness-to-width ratio, t/b, and different combinations of edge support conditions, are examined. The plate is modelled with 6 × 6, 9 × 9 and 16 × 16 distributed particles for QH8-R ($\alpha_0 = -0.17$) element.

Numerical results for thick plates with thickness-to-width ratios, $t/b = 0.05$, 0.1, skew angles, $\alpha = 0^\circ$, 15°, 30°, 45°, and various boundary conditions of $S^*S^*S^*S^*$, CCCC, CFCF, and S^*FS^*F, are compared with those of mesh-free method [48] (with 17×17 distributed particles) and Kitipornchai et al. [46] in Table 20. S^*, C, and F denote soft-type simply supported, clamped, and free boundary conditions, respectively. Based on the favorable comparisons observed in Table 8, it can be concluded that the plate buckling load intensity factors are well approximated by the QH8-R ($\alpha_0 = -0.17$) element.

4.3.3. A Square Plate with a Hole Subjected to Different In-Plane Loads. Lastly we consider a hard-type simply supported (SSSS) and clamped (CCCC) square plate with a hole. For the purpose of the comparison, the material parameters are taken the same as in the above example but the length $a = b = 10$ and the thickness $t = 1$ are employed instead. The irregularly scattered pattern of 84 elements and 308 nodes shown in Figure 21 is used. The plate is subjected to three different in-plane load cases, namely, an uniaxial compressive load in x-direction, σ_x^0, pure shear load, and biaxial compressive loads in x and y directions, where $\sigma_x{}^0 = \sigma_y{}^0$, respectively.

The results of the normalized buckling load factor calculated for those loads with different boundary conditions

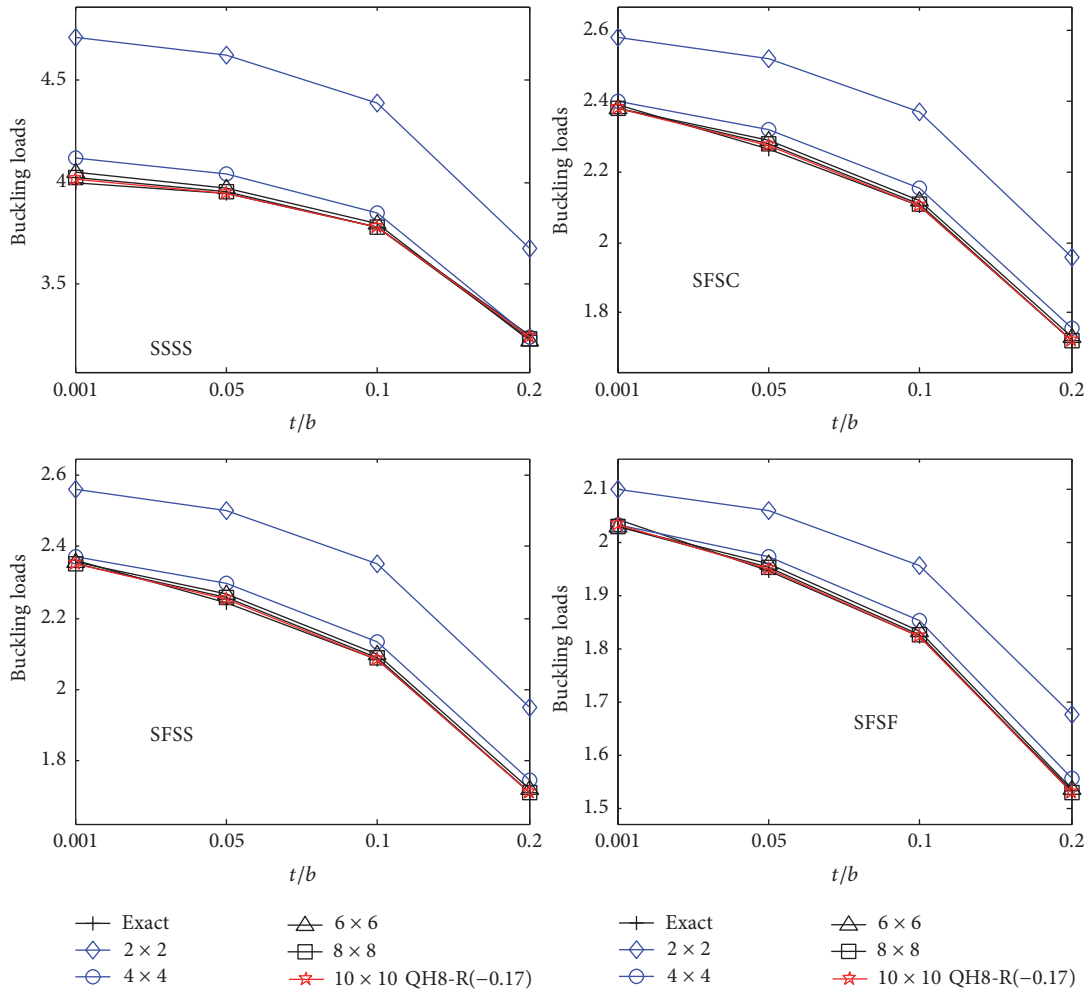

FIGURE 16: Normalized axial buckling load factors along the y-axis ($\sigma_y{}^0$) versus the thickness-span aspect ratio $t/b = 0.001, 0.05, 0.1, 0.2$ with various boundaries.

are shown in Table 21. The results agree very well with those computed by the EFG [57] involving both the third-order shear deformation plate theory (TSDT) and the FSDT. And the Shear-MK [55] with 400 nodes is also used for comparison. Additionally, it is also interesting to view the buckling modes of the problem and, thus, Figure 22 presents the first buckling modes under the three types of buckling loads for four different boundary conditions.

5. Conclusions

The higher-order hybrid stress quadrilateral Mindlin plate element QH8 for solving free vibration and buckling analysis problems is formulated in this paper. Due to numerical results given above, some concluding remarks can be drawn as follows.

The QH8 element is an efficiency method for solving the free vibration problems and buckling analysis of plate due to its high accuracy. It is free of shear locking and can pass both the constant bending with zero shear stresses and the strict patch test with nonzero constant shear stresses, no matter the element edges are straight or curved and no matter the shapes of the elements are convex or concave.

The refined nonconforming element method is a very efficient method, which can be used to improve the accuracy of nonconforming elements. It has been used to construct the QH8 element successfully. With the refined mass matrix and refined geometric stiffness matrix, the accuracy of vibration and stability analysis has been improved just by changing the value of α and α_0, and it really works.

From the numerical results, the present plate element has performed well in most situations. It is shown that the present plate element is applicable to either thin or thick situations with enough accuracy.

Conflicts of Interest

The authors declare that there are no conflicts of interest regarding the publication of this paper.

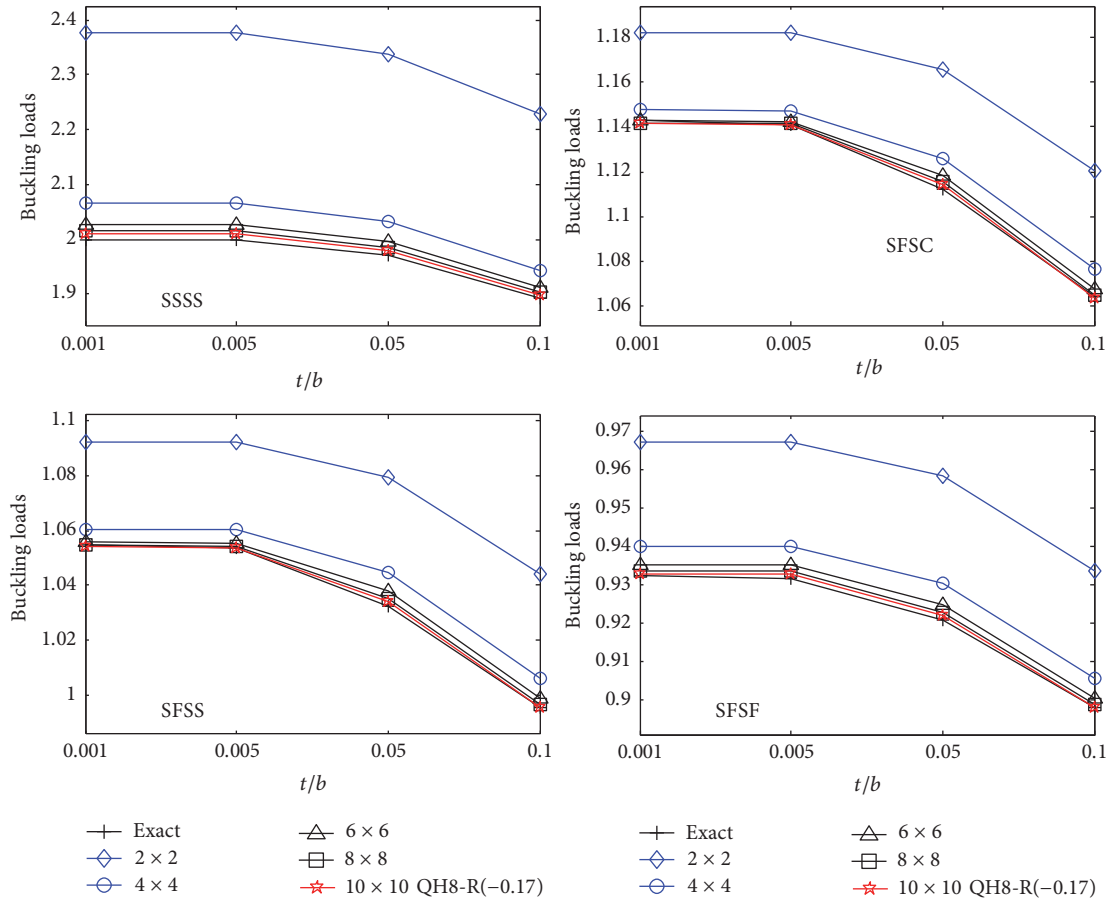

Figure 17: Normalized biaxial buckling load factors ($\sigma_x{}^0 = \sigma_y{}^0$) versus the thickness-span aspect ratio $t/b = 0.001, 0.05, 0.1, 0.2$ with various boundaries.

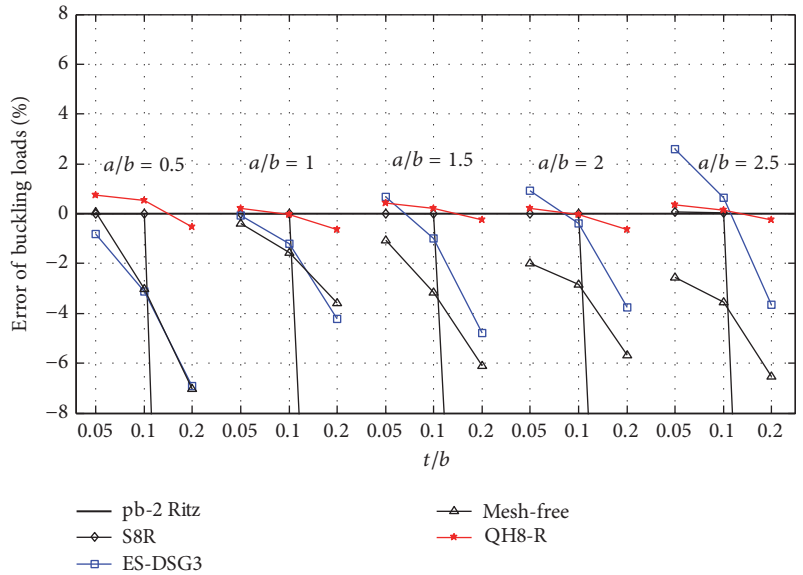

Figure 18: The factor of axial buckling loads of SSSS plates with various length-to-width ratios (a/b) and various thickness-to-width ratios (t/b).

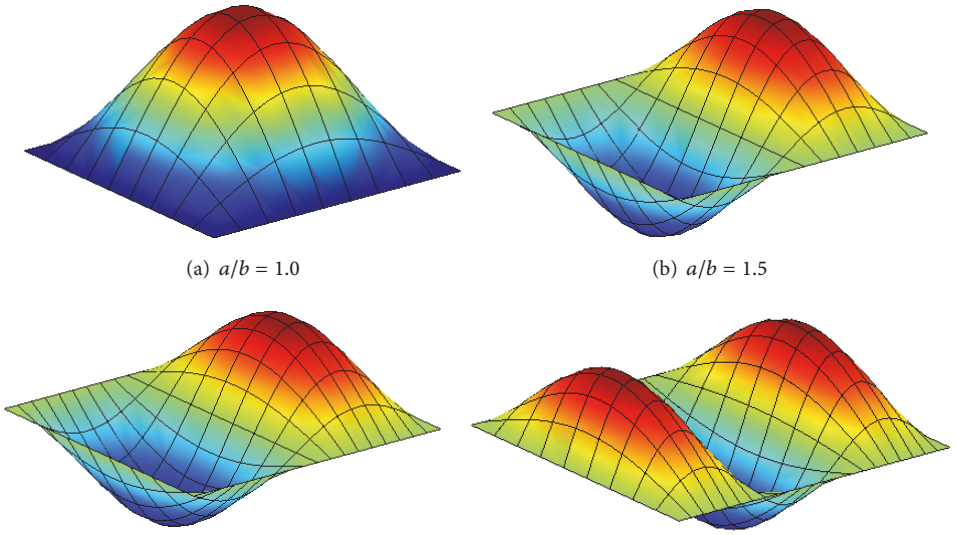

(a) $a/b = 1.0$ (b) $a/b = 1.5$

(c) $a/b = 2.0$ (d) $a/b = 2.5$

FIGURE 19: Axial buckling modes of simply supported rectangular plates with thickness-to-width ratios $t/b = 0.01$ and various length-to-width ratios a/b.

TABLE 16: The factor of uniaxial buckling loads ($\sigma_x{}^0$) along the x-axis of rectangular plates ($a/b = 1$) with various boundary conditions and various thickness-to-width ratios (t/b).

Boundary	Method	t/b			
		0.001	0.05	0.1	0.2
SSSS	SSM	4.000	3.944	3.784	3.256
	Shear-MK	4.0243	3.9153	3.7895	3.2748
	MK	5.467	5.0111	3.7905	3.2799
	Exact [45]	4.000	3.9437	3.7838	3.2558
	S8R	3.997	3.9445	3.7866	1.7025
	QH8-R	4.0132	3.9478	3.7827	3.2464
SFSC	SSM	1.653	1.620	1.556	1.370
	Shear-MK	1.6552	1.6211	1.5658	1.3765
	MK	2.5876	2.1778	1.5699	1.3612
	Exact [45]	1.6522	1.6197	1.5558	1.3701
	S8R	1.6560	1.6202	1.5570	1.2532
	QH8-R	1.6522	1.6209	1.5549	1.3669
SFSS	SSM	1.402	1.378	1.327	1.173
	Shear-MK	1.4211	1.3877	1.3795	1.2700
	MK	2.2456	2.0323	1.3791	1.2755
	Exact [45]	1.4014	1.3813	1.3707	1.2138
	S8R	1.4017	1.3816	1.3415	1.2158
	QH8-R	1.4022	1.3827	1.3410	1.2133
SFSF	SSM	0.9523	0.9412	0.9146	0.8274
	Shear-MK	0.9676	0.9455	0.9231	0.8575
	MK	1.7644	1.6578	0.9344	0.8654
	Exact [45]	0.95225	0.94314	0.92187	0.85011
	S8R	0.9524	0.9433	0.9223	0.8325
	QH8-R	0.9532	0.9442	0.9227	0.8519

Note. QH8-R ($\alpha_0 = -0.17$). Shear correction factor $\kappa = \pi^2/12$.

Table 17: The factor of uniaxial buckling loads ($\sigma_y{}^0$) along the y-axis of rectangular plates ($a/b = 1$) with various boundary conditions and various thickness-to-width ratios (t/b).

Boundary	Element	t/b			
		0.001	0.05	0.1	0.2
SSSS	2 × 2	4.7132	4.6261	4.3905	3.6771
	4 × 4	4.1193	4.0431	3.8479	3.2455
	6 × 6	4.0476	3.9751	3.7949	3.2231
	8 × 8	4.0257	3.9564	3.785	3.2321
	10 × 10	4.0161	3.9495	3.7829	3.2422
	Exact [45]	4.0000	3.9437	3.7838	3.2558
SFSC	2 × 2	2.5834	2.5216	2.3678	1.9583
	4 × 4	2.3993	2.3194	2.1530	1.7580
	6 × 6	2.3821	2.2898	2.1191	1.7288
	8 × 8	2.3797	2.2794	2.1079	1.7213
	10 × 10	2.3799	2.2743	2.1031	1.7190
	Exact [45]	2.3901	2.2667	2.1010	1.7200
SFSS	2 × 2	2.5626	2.502	2.3511	1.9480
	4 × 4	2.3741	2.2965	2.1346	1.7483
	6 × 6	2.3567	2.2672	2.1010	1.7195
	8 × 8	2.3541	2.2569	2.0901	1.7122
	10 × 10	2.3542	2.2518	2.0853	1.7099
	Exact [45]	2.3639	2.2442	2.0829	1.7105
SFSF	2 × 2	2.1000	2.058	1.9553	1.6775
	4 × 4	2.0327	1.9737	1.8516	1.5567
	6 × 6	2.0286	1.9589	1.8315	1.5358
	8 × 8	2.0295	1.9531	1.8244	1.5301
	10 × 10	2.0309	1.9500	1.8212	1.5282
	Exact [45]	2.0413	1.9457	1.8216	1.5333

Note. QH8-R ($\alpha_0 = -0.17$). Shear correction factor $\kappa = \pi^2/12$.

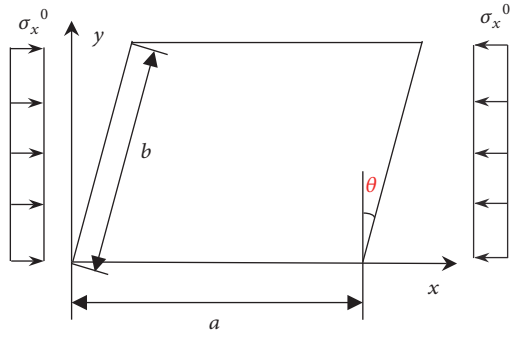

Figure 20: Skew plate under uniaxial in-plane loading.

Table 18: The factor of biaxial buckling loads ($\sigma_x^0 = \sigma_y^0$) for rectangular plates ($a/b = 1$) with various boundary conditions and various thickness-to-width ratios (t/b).

Boundary	Element	t/b			
		0.001	0.005	0.05	0.1
SSSS	2 × 2	2.3774	2.3770	2.3377	2.2277
	4 × 4	2.0671	2.0667	2.0334	1.9432
	6 × 6	2.0275	2.0272	1.9954	1.9108
	8 × 8	2.015	2.0147	1.984	1.9023
	10 × 10	2.0095	2.0091	1.9793	1.8992
	Exact [45][a]	2.0000	1.9997	1.9718	1.8919
SFSC	2 × 2	1.1820	1.1818	1.1652	1.1205
	4 × 4	1.1474	1.1472	1.1261	1.0767
	6 × 6	1.1427	1.1424	1.1184	1.0679
	8 × 8	1.1416	1.1413	1.1155	1.0649
	10 × 10	1.1414	1.1410	1.1140	1.0636
	Exact [45][b]	1.1431	1.1412	1.1119	1.0641
SFSS	2 × 2	1.0925	1.0923	1.0794	1.0439
	4 × 4	1.0606	1.0605	1.0445	1.0060
	6 × 6	1.0558	1.0556	1.0378	0.9986
	8 × 8	1.0546	1.0543	1.0352	0.9962
	10 × 10	1.0541	1.0538	1.0340	0.9952
	Exact [45][b]	1.0548	1.0535	1.0322	0.99541
SFSF	2 × 2	0.9671	0.9670	0.9583	0.9334
	4 × 4	0.9400	0.9399	0.9302	0.9053
	6 × 6	0.9351	0.9349	0.9247	0.9002
	8 × 8	0.9335	0.9333	0.9228	0.8986
	10 × 10	0.9328	0.9326	0.9219	0.8979
	Exact [45][b]	0.93209	0.9316	0.92071	0.89774

Note. QH8-R ($\alpha_0 = -0.17$). [a]Shear correction factor $\kappa = 0.823045$. [b]Shear correction factor $\kappa = 5/6$.

Table 19: The factor of uniaxial buckling loads along the x-axis of rectangular plates (SSSS) with various length-to-width ratios and various thickness-to-width ratios.

a/b	t/b	S8R	ES-DSG3 [47]	Mesh-free [48]	QH8-R	pb-2 Ritz [46]
0.5	0.05	6.0376	5.9873	6.0405	6.0822	6.0372
	0.1	5.4779	5.3064	5.3116	5.5071	5.4777
	0.2	1.9525	3.720	3.7157	3.9754	3.9963
1	0.05	3.9441	3.9412	3.9293	3.9528	3.9444
	0.1	3.7861	3.7402	3.7270	3.7855	3.7865
	0.2	2.0444	3.1263	3.1471	3.2427	3.2637
1.5	0.05	4.2576	4.2852	4.2116	4.2745	4.2570
	0.1	4.0255	3.9844	3.8982	4.0332	4.0250
	0.2	2.0132	3.1461	3.1032	3.2966	3.3048
2	0.05	3.9440	3.9811	3.8657	3.9528	3.9444
	0.1	3.7860	3.7711	3.6797	3.7855	3.7865
	0.2	1.9486	3.1415	3.0783	3.2427	3.2637
2.5	0.05	4.0673	4.1691	3.9600	4.0795	4.0645
	0.1	3.8700	3.8924	3.7311	3.8737	3.8683
	0.2	1.8697	3.1234	3.0306	3.2338	3.2421

Table 20: Buckling load intensity factor of skew plates having $S^*S^*S^*S^*$, CCCC, CFCF, and S^*FS^*F boundary conditions subject to uniaxial loads ($\sigma_x{}^0$).

Boundary	t/b	Skew angle	Mesh-free [48]	6×6	9×9	16×16	pb-2 Ritz [46]
$S^*S^*S^*S^*$	0.05	0°	—	3.8057	3.7905	3.7815	3.7835
		15°	—	4.1583	4.1380	4.1276	4.1314
		30°	5.3874	5.4755	5.4304	5.4109	5.4182
		45°	8.6926	8.9757	8.8002	8.7247	8.7328
	0.1	0°	—	3.5111	3.5007	3.4965	3.4950
		15°	—	3.8234	3.8094	3.8047	3.8027
		30°	4.8534	4.9813	4.9475	4.9370	4.9324
		45°	7.6106	7.9388	7.7931	7.7430	7.7236
CCCC	0.05	0°	9.5418	9.8091	9.6238	9.5647	9.5588
		15°	10.2123	10.5549	10.3209	10.2430	10.2312
		30°	12.5225	13.2413	12.7803	12.6114	12.5711
		45°	17.8211	19.9900	18.6615	18.1211	17.9652
	0.1	0°	8.1849	8.3903	8.2836	8.2936	8.2917
		15°	8.7560	8.9338	8.7863	8.7845	8.7741
		30°	10.3273	10.8235	10.4883	10.4238	10.3760
		45°	13.2881	15.2116	14.2092	13.8638	13.6909
CFCF	0.05	0°	3.7984	3.8724	3.8281	3.8082	3.8007
		15°	4.1310	4.2202	4.1688	4.1460	4.1387
		30°	5.3510	5.4976	5.4102	5.3720	5.3660
		45°	7.3658	7.9413	7.6341	7.4986	7.4670
	0.1	0°	3.5063	3.5523	3.5262	3.5185	3.5077
		15°	3.7684	3.8441	3.8135	3.8049	3.7937
		30°	4.7773	4.8862	4.8316	4.8168	4.8043
		45°	6.3092	6.6886	6.4547	6.3680	6.3311
S^*FS^*F	0.05	0°	—	0.9459	0.9436	0.9424	0.9421
		15°	—	1.0535	1.0513	1.0501	1.0501
		30°	—	1.4612	1.4594	1.4583	1.4603
		45°	—	2.5333	2.5317	2.5311	2.5450
	0.1	0°	—	0.9227	0.9210	0.9202	0.9199
		15°	—	1.0215	1.0199	1.0191	1.0189
		30°	—	1.3892	1.3878	1.3873	1.3887
		45°	—	2.3192	2.3187	2.3190	2.3316

Note. 6×6, 9×9, 16×16: the meshes for element QH8-R(−0.17).

Table 21: The uniaxial, biaxial, and pure shear buckling load factor for a square plate with a circular hole and different boundary conditions.

Buckling load	Boundary	EFG (FSDT)	EFG (TSDT)	Shear-MK	HQ8-R
Uniaxial	CCCC	7.995	8.097	8.0777	8.0543
	SSSS	1.986	1.969	1.9544	2.0580
Biaxial	CCCC	4.781	4.860	4.9878	4.8477
	SSSS	1.032	1.021	1.0511	1.0696
Pure shear	CCCC	12.669	13.357	13.5252	12.6976
	SSSS	7.867	7.873	8.1544	7.8971

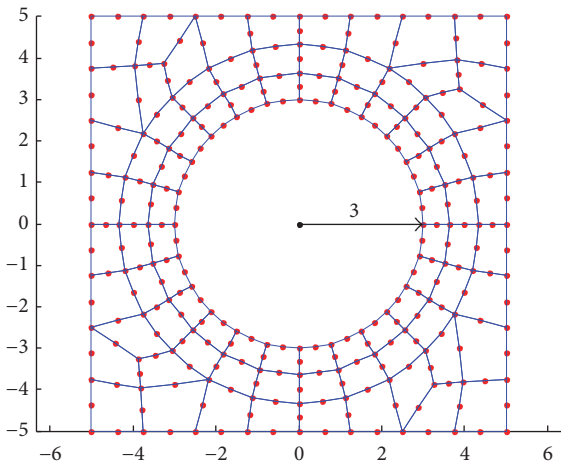

Figure 21: Square plate with a circular hole and the distributions (308 nodes, 84 elements).

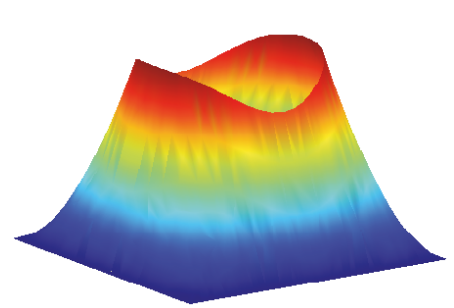

(a) Uniaxial SSSS

(b) Uniaxial CCCC

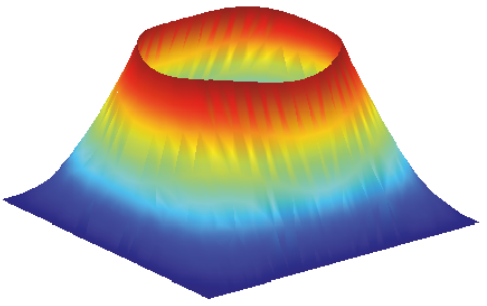

(c) Biaxial SSSS

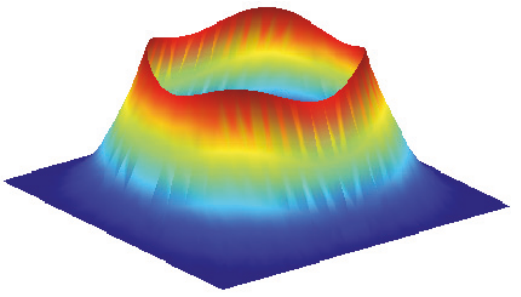

(d) Biaxial CCCC

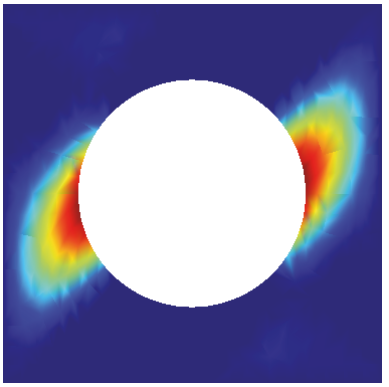

(e) Pure shear SSSS

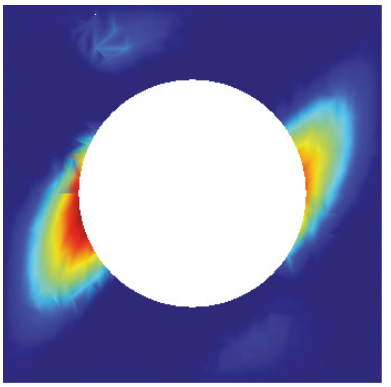

(f) Pure shear CCCC

Figure 22: The first uniaxial, biaxial, and pear shear buckling modes of the plate with a circular hole associated with different boundaries as SSSS, CCCC (thickness $t = 1.0$).

Acknowledgments

The work in this paper was supported by the National Natural Sciences Foundations of China (no. 11702242 and no. 11572204), Youth Foundation of Hebei Educational Committee (QN2017151), and Foundations of Yanshan University (no. 15LGB020, no. 16LGB015, no. B922, and no. B981). Those grants are gratefully acknowledged.

References

[1] M. Wang, "On the necessity and sufficiency of the patch test for convergence of nonconforming finite elements," *SIAM Journal on Numerical Analysis*, vol. 39, no. 2, pp. 363–384, 2001.

[2] S. Cen and Y. Shang, "Developments of Mindlin-Reissner plate elements," *Mathematical Problems in Engineering*, vol. 2015, Article ID 456740, 2015.

[3] J. Robinson and G. W. Haggenmacher, "LORA-an accurate four node stress plate bending element," *International Journal for Numerical Methods in Engineering*, vol. 14, no. 2, pp. 296–306, 1979.

[4] E. Hinton and H. C. Huang, "A family of quadrilateral Mindlin plate elements with substitute shear strain fields," *Computers & Structures*, vol. 23, no. 3, pp. 409–431, 1986.

[5] O. C. Zienkiewicz, R. L. Taylor, and J. M. Too, "Reduced integration technique in general analysis of plates and shells," *International Journal for Numerical Methods in Engineering*, vol. 3, no. 2, pp. 275–290, 1971.

[6] E. D. L. Pugh, E. Hinton, and O. C. Zienkiewicz, "A study of quadrilateral plate bending elements with 'reduced' integration," *International Journal for Numerical Methods in Engineering*, vol. 12, no. 7, pp. 1059–1079, 1978.

[7] T. J. R. Hughes, M. Cohen, and M. Haroun, "Reduced and selective integration techniques in the finite element analysis of plates," *Nuclear Engineering and Design*, vol. 46, no. 1, pp. 203–222, 1978.

[8] T. J. R. Hughes and T. E. Tezduyar, "Finite elements based upon Mindlin plate theory with particular reference to the four-node bilinear isoparametric element," *Transactions ASME—Journal of Applied Mechanics*, vol. 48, no. 3, pp. 587–596, 1981.

[9] T. Belytschko, C. S. Tsay, and W. K. Liu, "A stabilization matrix for the bilinear Mindlin plate element," *Computer Methods Applied Mechanics and Engineering*, vol. 29, no. 3, pp. 313–327, 1981.

[10] J.-L. Batoz and P. Lardeur, "A discrete shear triangular nine d.o.f. element for the analysis of thick to very thin plates," *International Journal for Numerical Methods in Engineering*, vol. 28, no. 3, pp. 533–560, 1989.

[11] J.-L. Batoz and I. Katili, "On a simple triangular reissner/mindlin plate element based on incompatible modes and discrete constraints," *International Journal for Numerical Methods in Engineering*, vol. 35, no. 8, pp. 1603–1632, 1992.

[12] K.-J. Bathe, A. Iosilevich, and D. Chapelle, "Evaluation of the MITC shell elements," *Computers & Structures*, vol. 75, no. 1, pp. 1–30, 2000.

[13] A. K. Soh, Z. F. Long, and S. Cen, "A new nine dof triangular element for analysis of thick and thin plates," *Computational Mechanics*, vol. 24, no. 5, pp. 408–417, 1999.

[14] A.-K. Soh, S. Cen, Y.-Q. Long, and Z.-F. Long, "A new twelve DOF quadrilateral element for analysis of thick and thin plates," *European Journal of Mechanics - A/Solids*, vol. 20, no. 2, pp. 299–326, 2001.

[15] C. Wanji and Y. K. Cheung, "Refined quadrilateral element based on Mindlin/Reissner plate theory," *International Journal for Numerical Methods in Engineering*, vol. 47, no. 1-3, pp. 605–627, 2000.

[16] C. Wanji and Y. K. Cheung, "Refined 9-Dof triangular Mindlin plate elements," *International Journal for Numerical Methods in Engineering*, vol. 51, no. 11, pp. 1259–1282, 2001.

[17] S. Cen, Y.-Q. Long, Z.-H. Yao, and S.-P. Chiew, "Application of the quadrilateral area co-ordinate method: a new element for Mindlin-Reissner plate," *International Journal for Numerical Methods in Engineering*, vol. 66, no. 1, pp. 1–45, 2006.

[18] C. Wang, X. Wang, X. Zhang, and P. Hu, "Assumed stress quasi-conforming technique for static and free vibration analysis of Reissner-Mindlin plates," *International Journal for Numerical Methods in Engineering*, 2017.

[19] W. Chen, "Enhanced patch test of finite element methods," *Science China Physics, Mechanics & Astronomy*, vol. 49, no. 2, pp. 213–227, 2006.

[20] W. Chen, J. Wang, and J. Zhao, "Functions for patch test in finite element analysis of the Mindlin plate and the thin cylindrical shell," *Science China Physics, Mechanics & Astronomy*, vol. 52, no. 5, pp. 762–767, 2009.

[21] G. Jelenić and E. Papa, "Exact solution of 3D Timoshenko beam problem using linked interpolation of arbitrary order," *Archive of Applied Mechanics*, vol. 81, no. 2, pp. 171–183, 2011.

[22] T. Li, X. Ma, J. Xili, and W. Chen, "Higher-order hybrid stress triangular Mindlin plate element," *Computational Mechanics*, vol. 58, no. 6, pp. 911–928, 2016.

[23] T. Li, Z. Qi, X. Ma, and W. Chen, "Higher-order assumed stress quadrilateral element for the Mindlin plate bending problem," *Structural Engineering and Mechanics*, vol. 54, no. 3, pp. 393–417, 2015.

[24] W. J. Chen and Y. K. Cheung, "The Non-Conforming Nine-Parameters Triangular Element for Thin Plate Bending and Vibration Analysis," in *Proc. COCMSGE*, P. K. K. Lee, L. G. Than, and Y. K. Cheung, Eds., pp. 1580–1583, Hong Kong, December 1994.

[25] Y. K. Cheung and W. J. Chen, "Refined nine-parameter triangular thin plate bending element by using refined direct stiffness method," *International Journal for Numerical Methods in Engineering*, vol. 38, no. 2, pp. 283–298, 1995.

[26] X. Ma and W. Chen, "Refined 18-DOF triangular hybrid stress element for couple stress theory," *Finite Elements in Analysis and Design*, vol. 75, pp. 8–18, 2013.

[27] K. M. Liew, K. C. Hung, and M. K. Lim, "Vibration of mindlin plates using boundary characteristic orthogonal polynomials," *Journal of Sound and Vibration*, vol. 182, no. 1, pp. 77–90, 1995.

[28] T. H. H. Pian, "Derivation of element stiffness matrices by assumed stress distributions," *AIAA Journal*, vol. 2, no. 7, pp. 1333–1336, 1964.

[29] T. H. H. Pian, "Element stiffness matrices for boundary compatibility and for prescribed boundary stresses," in *Proceedings of the 1st Conf. on Matrix Methods in Struct*, pp. 457–477, 1965.

[30] D. S. Malkus and T. J. R. Hughes, "Mixed finite element methods—reduced and selective integration techniques: a unification of concepts," *Computer Methods Applied Mechanics and Engineering*, vol. 15, no. 1, pp. 63–81, 1978.

[31] P. Tong, "A family of hybrid plate elements," *International Journal for Numerical Methods in Engineering*, vol. 18, no. 10, pp. 1455–1468, 1982.

[32] K. Y. Sze, Q. H. Zhang, and G. H. Liu, "Hybrid quadrilateral finite element models for axial symmetric Helmholtz problem," *Finite Elements in Analysis and Design*, vol. 52, pp. 1–10, 2012.

[33] H. A. Santos and J. P. Moitinho de Almeida, "A family of Piola-Kirchhoff hybrid stress finite elements for two-dimensional linear elasticity," *Finite Elements in Analysis and Design*, vol. 85, pp. 33–49, 2014.

[34] R. E. Erkmen, "Shear deformable hybrid finite-element formulation for buckling analysis of thin-walled members," *Finite Elements in Analysis and Design*, vol. 82, pp. 32–45, 2014.

[35] T. Nishioka and S. N. Atluri, "Assumed stress finite element analysis of through-cracks in angle-ply laminates," *AIAA Journal*, vol. 18, no. 9, pp. 1125–1132, 1980.

[36] J. P. Wolf, "Structural averaging of stresses in the hybrid stress model," *Aiaa Journal*, vol. 10, no. 6, pp. 843–845, 2015.

[37] P. Tong, "New displacement hybrid finite element models for solid continua," *International Journal for Numerical Methods in Engineering*, vol. 2, no. 1, pp. 73–83, 1970.

[38] K.-J. Bathe and E. N. Dvorkin, "A four-node plate bending element based on Mindlin/Reissner plate theory and a mixed interpolation," *International Journal for Numerical Methods in Engineering*, vol. 21, no. 2, pp. 367–383, 1985.

[39] R. Ayad, G. Dhatt, and J. L. Batoz, "A new hybrid-mixed variational approach for Reissner-Mindlin plates, The MISP model," *International Journal for Numerical Methods in Engineering*, vol. 42, no. 7, pp. 1149–1179, 1998.

[40] S. Brasile, "An isostatic assumed stress triangular element for the Reissner-Mindlin plate-bending problem," *International Journal for Numerical Methods in Engineering*, vol. 74, no. 6, pp. 971–995, 2008.

[41] A. K. Soh, L. Zhifei, and C. Song, "A Mindlin plate triangular element with improved interpolation based on Timoshenko's beam theory," *Communications in Numerical Methods in Engineering*, vol. 15, no. 7, pp. 527–532, 1999.

[42] A. W. Leissa, *Vibration of Plates*, National Aeronautics and Space Administration, Washington DC, Wash, USA, 1969.

[43] T. Irie, G. Yamada, and S. Aomura, "Natural frequencies of mindlin circular plates," *Journal of Applied Mechanics*, vol. 47, no. 3, pp. 652–655, 1980.

[44] S. P. Timoshenko and J. M. Gere, *Theory of Elastic Stability*, McGraw-Hill, New York, NY, USA, 1970.

[45] S. Hosseini-Hashemi, K. Khorshidi, and M. Amabili, "Exact solution for linear buckling of rectangular Mindlin plates," *Journal of Sound and Vibration*, vol. 315, no. 1-2, pp. 318–342, 2008.

[46] S. Kitipornchai, Y. Xiang, C. M. Wang, and K. M. Liew, "Buckling of thick skew plates," *International Journal for Numerical Methods in Engineering*, vol. 36, no. 8, pp. 1299–1310, 1993.

[47] H. Nguyen-Xuan, G. R. Liu, C. Thai-Hoang, and T. Nguyen-Thoi, "An edge-based smoothed finite element method (ES-FEM) with stabilized discrete shear gap technique for analysis of Reissner-Mindlin plates," *Computer Methods Applied Mechanics and Engineering*, vol. 199, no. 9-12, pp. 471–489, 2010.

[48] K. M. Liew, J. Wang, T. Y. Ng, and M. J. Tan, "Free vibration and buckling analyses of shear-deformable plates based on FSDT meshfree method," *Journal of Sound and Vibration*, vol. 276, no. 3-5, pp. 997–1017, 2004.

[49] H. Sofuoglu and H. Gedikli, "A refined 5-node plate bending element based on Reissner-Mindlin theory," *Communications in Numerical Methods in Engineering*, vol. 23, no. 5, pp. 385–403, 2007.

[50] E. Hinton, T. Rock, and O. C. Zienkiewicz, "A note on mass lumping and related processes in the finite element method," *Earthquake Engineering & Structural Dynamics*, vol. 4, no. 3, pp. 245–249, 1976.

[51] F. Wu, G. R. Liu, G. Y. Li, A. G. Cheng, and Z. C. He, "A new hybrid smoothed FEM for static and free vibration analyses of Reissner-Mindlin Plates," *Computational Mechanics*, 2014.

[52] S. J. Lee, "Free vibration analysis of plates by using a four-node finite element formulated with assumed natural transverse shear strain," *Journal of Sound and Vibration*, vol. 278, no. 3, pp. 657–684, 2004.

[53] O. G. McGee, A. W. Leissa, and C. S. Huang, "Vibrations of cantilevered skewed trapezoidal and triangular plates with corner stress singularities," *International Journal of Mechanical Sciences*, vol. 34, no. 1, pp. 63–84, 1992.

[54] T. Mlzusawa, "Vibration of rectangular mindlin plates with tapered thickness by the spline strip method," *Computers & Structures*, vol. 46, no. 3, pp. 451–463, 1993.

[55] T. Q. Bui, M. N. Nguyen, and C. Zhang, "Buckling analysis of Reissner-Mindlin plates subjected to in-plane edge loads using a shear-locking-free and meshfree method," *Engineering Analysis with Boundary Elements*, vol. 35, no. 9, pp. 1038–1053, 2011.

[56] C. M. Wang, S. Kitipornchai, Y. Xiang, and K. M. Liew, "Stability of skew mindlin plates under isotropic in-plane pressure," *Journal of Engineering Mechanics*, vol. 119, no. 2, pp. 393–401, 1993.

[57] S. F. Li and W. K. Liu, *Meshfree Particle Method*, Springer, Berlin, Heidelberg, NY, 2004.